J. Fluid Mech. (1986), vol. 162, pp. 299–338
Printed in Great Britain

The evolution of grid-generated turbulence in a stably stratified fluid

By E. C. ITSWEIRE†, K. N. HELLAND AND C. W. VAN ATTA‡
Department of Applied Mechanics and Engineering Sciences and Institute for Pure and Applied Physical Sciences, University of California, San Diego, La Jolla, CA 92093

(Received 25 January 1985 and in revised form 1 August 1985)

The spatial decay and structural evolution of grid-generated turbulence under the effect of buoyancy was studied in a ten-layer, salt-stratified water channel. The various density gradients were chosen such that the initial overturning turbulent scale was slightly smaller than any of the respective buoyancy scales. The observed general evolution of the flow from homogeneous turbulence to a composite of fossil turbulence or quasi-two-dimensional turbulence and internal wavefield is in good agreement with the predictions of Gibson (1980) and the lengthscale model of Stillinger, Helland & Van Atta (1983). The effect of the initial size of the turbulent lengthscale compared with the buoyancy scale on the decay and evolution of the turbulence is investigated and the observed influence on the rate of decay of both longitudinal and vertical velocity fluctuations pointed out by Van Atta, Helland & Itsweire (1984) is shown to be related to the magnitude of the initial internal wavefield at the grid. An attempt is made to remove the wave-component kinetic energy from the vertical-velocity-fluctuation data of Stillinger, Helland & Van Atta (1983) in order to obtain the true decay of the turbulent fluctuations. The evolution of the resulting fluctuations is similar to that of the present large-grid data and several towed-grid experiments. The rate of destruction of the density fluctuations (active-scalar dissipation rate) is estimated from the evolution equation for the potential energy, and the deduced Cox numbers are compared with those obtained from oceanic microstructure measurements. The classical Kolmogorov and Batchelor scalings appear to collapse the velocity and density spectra better than the buoyancy scaling proposed by Gargett, Osborn & Nasmyth (1984). The rise of the velocity spectra at low wavenumbers found by Stillinger, Helland & Van Atta (1983) is shown to be related to internal waves.

1. Introduction

A number of laboratory experiments in stably stratified turbulent flows have been conducted during the last decade to try to quantify the dynamical effects of buoyancy forces on turbulent mixing. However, even for the simplest zero-shear experiments, i.e. turbulence downstream of a biplane grid, the behaviour of such quantities as the velocity and density fluctuations, and their spectral shapes is not well understood. Several scenarios have been proposed to explain the very different behaviour of the velocity fluctuations in different experiments.

Some experiments have been conducted in wind tunnels using temperature as the

† Also Mechanical Engineering, University of California, Irvine.
‡ Also Scripps Institution of Oceanography.

stratifying agent (Montgomery 1974; Sirivat & Warhaft 1983) but the temperature gradients involved were too small to produce any substantial buoyancy forces that could compete with the inertial and viscous forces. These experiments are useful for defining the limiting case of passive-scalar behaviour with Prandtl number of order one. Active-scalar (buoyancy) effects have been obtained in experiments performed in water with salt as the stratifying agent.

First, Lin & Veenhuizen (1975) towed an array of vertical rods (they avoided horizontal rods in order to reduce possible internal-wave generation by the wakes of these rods) in a linearly stratified fluid. Their main conclusion was that buoyancy forces simply increased the rate of decay of the vertical velocity fluctuations compared with the non-stratified fluid. Britter *et al.* (1983) conducted some similar experiments behind a biplane grid and their velocity measurements also showed that the main effect of buoyancy forces was to suppress the vertical velocity component. In both cases, the selected density gradients were large enough that the flow was always dynamically dominated by buoyancy throughout its entire history.

Dickey & Mellor (1980) dropped a biplane grid through a stratified fluid of constant density gradient and observed that initially both transverse and vertical turbulent-velocity intensities were unaffected by buoyancy, i.e. they followed the same decay rate as in the neutral case. Then, for longer times both turbulent-velocity intensities oscillated around some nearly constant level which they interpreted as corresponding to an internal wavefield. Recently, Stillinger, Helland & Van Atta (1983*b*, hereinafter referred to as SHV), using a continuously stratified water channel, measured longitudinal and vertical velocities and density behind a biplane grid. Their measurements showed a behaviour similar in some respects to Dickey & Mellor (1980), allowing a similar interpretation concerning the onset of buoyancy forces on the initially isotropic turbulence.

In all these experiments, the initial turbulent scale, density gradient, facility and instrumentation were widely different. In the present study, we sought to vary only one of these parameters, viz. the grid mesh size M and therefore the initial turbulent lengthscale, while using the same facility and instrumentation as SHV in order to try to resolve some of the discrepancies between the previously mentioned experiments.

Most of the experiments mentioned above did not provide any detailed data for the concurrent behaviour of the density fluctuations. Lange (1982) measured the density fluctuations behind his towed grid but did not report any velocity measurements. SHV used their density-fluctuation measurements to calculate an overturning lengthscale and deduced a buoyancy criterion for the extinction of turbulent motions. Rohr, Itsweire & Van Atta (1984) recast these two quantities in terms of the mixing efficiency of the flow, but they did not try to estimate the rate of destruction of the density fluctuations χ, which is important for using the results of controlled laboratory experiments as a framework for possible interpretations of the dynamics of oceanic microstructure (Gregg 1980; Dillon & Caldwell 1980; Gibson 1982*a*). The primary variables measured in the ocean are salinity and temperature fluctuations (and therefore density fluctuations) and their vertical gradients. In the laboratory, salinity-gradient fluctuations contributing to χ are of too small a scale to be resolved by existing conductivity probes (Head 1983) but χ can be estimated indirectly by measuring the other terms in the equation for the evolution of fluctuating potential energy (r.m.s. density fluctuations). All of the other terms can be measured for the present laterally homogeneous and uniform turbulent flow. The shape of density spectra can also be compared with theoretical two-dimensional and fossil turbulent spectra to further characterize the final state of motion far from the grid.

Some of the spectral properties of a decaying velocity field in a stratified flow were discussed by SHV who compared velocity spectra in the stratified flow at several downstream locations with unstratified measurements in the same facility. They concluded that the vertical velocity spectra non-dimensionalized by the Kolmogorov scales were in good agreement with non-stratified water-channel and wind-tunnel measurements for most wavenumbers for small x/M, e.g. for x/M sufficiently small that the flow was in the region of overturning turbulence. For larger downstream locations, the velocity spectra deviated systematically from the universal spectral form. We have further examined the velocity spectra of SHV as well as the velocity spectra of the new data. In addition we have considered the behaviour of the density spectra and made comparisons between kinetic- and potential-energy spectra in the wave-dominated region of the decay. The buoyancy scaling proposed by Gargett, Osborn & Nasmyth (1984) was tried along with the Kolmogorov and Batchelor scalings.

2. Experimental set-up

The experiments were carried out in the closed-loop, gravity-driven, ten-layer salt-stratified water channel in the department of Applied Mechanics and Engineering Sciences at the University of California, San Diego. This channel, previously described in detail by Stillinger *et al.* (1983*a*), has a test section of 25 cm × 40 cm × 5 m. The velocity profile in the present experiments was set to be uniform with an average mean speed $\bar{U} = 25$ cm/s.

Most of the present measurements (R36 and R37) were taken along the centreline of the channel at various locations downstream of a classical biplane grid with a mesh size $M = 3.81$ cm. The grid was made of cylindrical stainless-steel rods of diameter $d = 0.635$ cm, yielding a solidity $\sigma = 31\,\%$. The dimensions of the grid were chosen to double the mesh size of SHV while keeping the same solidity. The grid Reynolds number $R_e = UM/\nu$ was approximately 9500. The range of Brunt–Väisälä frequencies $N = [(g/\bar{\rho})(\partial\bar{\rho}/\partial z)]^{\frac{1}{2}}$ (rad/s) in this investigation was from $N = 0.24$ to 0.97 rad/s, including also the neutral case ($N = 0$), which provided a reference for the rate of decay of the vertical and longitudinal turbulent intensities in a non-stratified environment.

Three different probes were used for the velocity and density measurements. Quartz-coated TSI films mounted on an X-film probe provided measurements of the downstream (u) and vertical (w) velocity components, while a four-wire microscale conductivity instrument (MSCI) developed by Head (1983) gave the instantaneous conductivity and hence density of the salt solution. The hot films were standard TSI quartz-coated cylindrical sensors for use in salt water with 50 μm diameter and 1 mm sensing length. The distance between the outside electrodes of the four-wire MSCI was less than 0.75 mm and the horizontal separation between the X-film and the MSCI was less than 1 mm. The measuring volume of the combined X-film and MSCI sensors (≈ 1.5 mm) was of the order of the Kolmogorov scale and ten times smaller than the energy-containing eddies. A platinum resistance thermometer (PRT) measured the mean temperature variations required to compensate for the overheat changes of the films and to convert conductivity to density. No small-scale temperature fluctuations were created or observed. The mean temperature increase due to pump losses and viscous dissipation was about 1 °C/h and hot-film overheats varied from 12 to 8 °C from the beginning to the end of an experiment.

The X-films were calibrated by towing the instrumentation cart at a monotonically

increasing speed through the still water of the test section. The range of speeds attained was from 10 to 45 cm/s. Several tows were made before and after an experiment at yaw angles of 0° and ± 10°. This range is appropriate for low-intensity grid-generated turbulence. The MSCI was calibrated by dipping the instrument tip in two calibrated salt solutions before and after the runs. The modified King's law proposed by Castaldini, Helland & Malvestuto (1980) satisfactorily described the heat-transfer law of the hot films:

$$\frac{E_b^2}{T_f - T} = A + B\left(\frac{U}{\rho}\right)^n, \tag{1}$$

where E_b is the bridge voltage, U, ρ and T the velocity, density and ambient temperature of the salt solution and T_f the film temperature. The calibration constants A and B were found to be about 0 and 2 respectively, while the exponent n varied between 0.25 and 0.30 for different films. The impedance between each film and the salt solution was measured to be greater than 20 MΩ. Such a large value is required in order to avoid erratic behaviour and consequent errors in the calibrations and measurements. Using the error analysis of Stillinger (1983), temperature and salinity contaminations of the velocity components were found negligible. From (1) two *linearized* voltages were computed as:

$$E_l = \left(\frac{E_b^2/(T_f - T) - A}{B}\right)^{1/n}. \tag{2}$$

Assuming a cosine law appropriate for low-intensity turbulence, a first-order two-dimensional least-square fit was performed in terms of the *linearized* voltages. The u and w components were:

$$\left.\begin{aligned} u &= P_1 + Q_1 E_{l1} + R_1 E_{l2}; \\ w &= P_2 + Q_2 E_{l1} + R_2 E_{l2}. \end{aligned}\right\} \tag{3}$$

The subsequent calibration coefficients Q_1, R_1, Q_2 and R_2 were between 0.43 and 0.58. Such substantial departures from the 0.50 values for identical films at 45° are primarily due to uncertainties in the determination of the film-resistivity coefficients α. Since we used a small overheat (10–12 °C) in order to reduce bubble growth on the films, a small error in α can result in a sizeable sensitivity difference between the two films. The film temperatures calculated from the pre- and post-calibrations using (1) can differ from the preset film temperatures by several degrees. It has been observed that, when both preset and calculated film temperatures for each film are within 0.5 °C, the calibration coefficients for u and w are very close to ± 0.5.

3. Theoretical framework for stratified turbulent flows

3.1. *Characteristic lengthscales*

By dimensional analysis, Ozmidov (1965) and others derived a lengthscale, the Ozmidov scale $L_O = (\epsilon/N^3)^{\frac{1}{2}}$, at which the buoyancy forces are equal to the inertial forces. This lengthscale is in fact the largest possible turbulent scale allowed by buoyancy forces (within a scaling factor of order 1). Any motion larger than this scale would not be able to overturn and would be restricted to oscillating or wave-like motions. Another buoyancy lengthscale representative of the vertical displacements in a stable density gradient can be defined as $L_b = w'/N$. L_b is the vertical distance

Lengthscale	Symbol	Definition	Physical description
Ozmidov scale	L_O	$(\epsilon/N^3)^{\frac{1}{2}}$	Scale at which buoyancy forces equal inertial forces
Buoyancy scale	L_b	w'/N	Vertical distance travelled by a fluid particle in converting all its vertical kinetic energy into potential energy
Kolmogorov scale	L_K	$(\nu^3/\epsilon)^{\frac{1}{4}}$	Scale at which viscous forces equal inertial forces
Turbulent scale	L_t	$\rho'/(\partial\bar{\rho}/\partial z)$	Typical vertical distance travelled by fluid particles before either returning to their equilibrium level or mixing
Thorpe scale	L_T	$\langle d(z)^2\rangle^{\frac{1}{2}}$	Root mean square of the Thorpe displacements $d(z)$ measured from instantaneous density profiles

TABLE 1. Definition of the lengthscales characteristic of stably stratified turbulent flows

travelled by a fluid particle in converting all its vertical fluctuating kinetic energy into potential energy in a fluid of Brunt–Väisälä frequency N. Again L_b represents the largest vertical scale allowed by buoyancy since only a fraction of the vertical kinetic energy is usually converted into potential energy. The buoyancy scale L_b can easily be measured by horizontally moving probes. It will be shown in §4.1 that L_b includes contributions from internal waves whereas L_O is virtually free from internal-wave contributions. An analysis similar to the one used to obtain the Ozmidov scale L_O can be used to define the Kolmogorov scale $L_K = (\nu^3/\epsilon)^{\frac{1}{4}}$ as the scale at which turbulent motions are damped by viscous forces. Table 1 summarizes the definition and physical meaning of the lengthscales used in the present analysis. We know that the range of possible turbulent scales will be bounded by the Ozmidov scale at the high end and the Kolmogorov scale at the low end with some proportionality factors to be determined theoretically or experimentally.

Gibson (1980) predicted the range of possible overturning turbulent scales (in the three-dimensional, Kolmogorovian sense) to be:

$$1.2L_O \geqslant \lambda \geqslant 15L_K, \tag{4}$$

where $L_O = (\epsilon/N^3)^{\frac{1}{2}}$ is the Ozmidov scale, $L_K = (\nu^3/\epsilon)^{\frac{1}{4}}$ the Kolmogorov scale and λ a turbulent wavelength. Independently, Stillinger (1981) and Stillinger *et al.* (1983*b*) found that for laboratory stratified grid-generated turbulence the range of turbulent scales was:

$$1.4L_O \geqslant \lambda \geqslant 15.5L_K. \tag{5}$$

They defined the largest turbulent scale (in a statistical sense) of their flow as $2L_t$, where

$$L_t = \frac{\rho'}{\partial\bar{\rho}/\partial z}, \tag{6}$$

where ρ' is the root-mean-square density fluctuation. L_t was first introduced by Ellison (1957) as a typical vertical distance travelled by fluid particles before either returning towards their equilibrium level or mixing. It is a statistical vertical

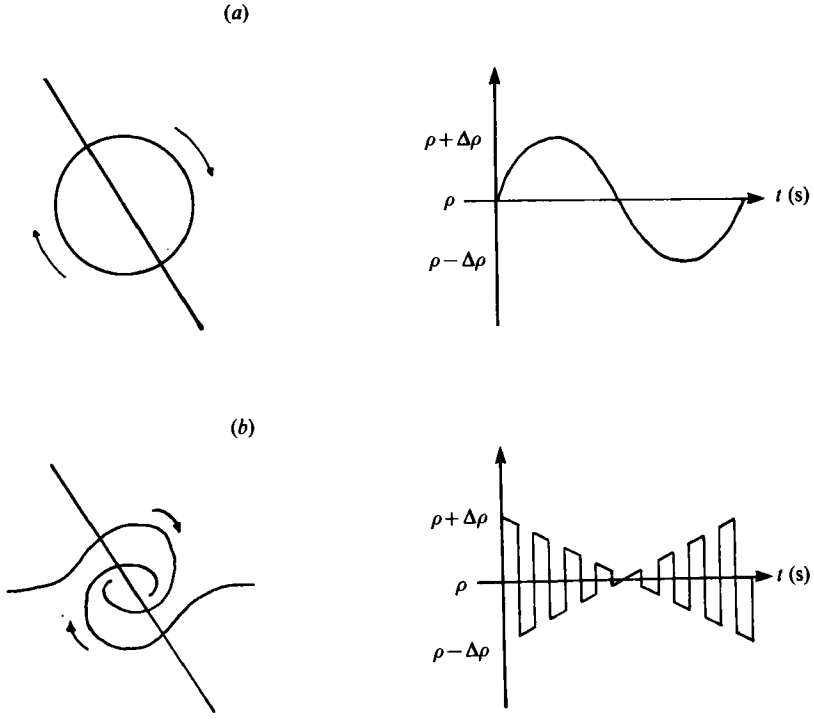

FIGURE 1. Turbulent-eddy model in a linear density gradient; (*a*) solid-body-rotation model; (*b*) shear-instability model.

turbulent scale that can be directly measured from stationary or horizontally towed conductivity probes and is probably proportional to the *largest* turbulent scale. SHV chose a scale factor of 2 to represent their *largest* turbulence scale using the simple solid-body-rotation model for turbulent eddies shown in figure 1. Such a representation is physically oversimplified but nevertheless seems to give a good estimate of the *largest* turbulent eddy size. As pointed out by Rohr *et al.* (1984) and Gargett *et al.* (1984), a perhaps preferable scale factor more consistent with the solid-body-rotation model would be $2\sqrt{2}$ instead of 2. Following the same idea that, in a stable constant density gradient, the density fluctuations may be simply related to the vertical turbulent motions, one can propose another estimate of the *largest* turbulent scale based on a shear-instability argument. From the instantaneous density profile through such an eddy (Gibson 1982*b*) shown in figure 1, the largest eddy size would be equal to $2\sqrt{3}\,L_t$. It is possible to introduce different multipliers relating the *largest* turbulent scale to L_t depending on the choice of the eddy model, and presumably the multiplier would depend on the nature of the generating mechanism for the turbulence, i.e. grid, shear instability, boundary layer or wake.

Strictly speaking the *largest* overturns can only be measured from instantaneous vertical density profiles in the ocean and lakes (Thorpe 1977; Dillon 1982) or in the laboratory (Itsweire 1984). Thorpe's (1977) method for estimating vertical displacements in a horizontally homogeneous stratified turbulent flow consists of reordering a measured instantaneous density profile, which contains density inversions, into a monotonic stable profile, i.e. a profile of minimum potential energy. Thorpe displacements $d(z)$ are the vertical distances individual fluid particles have to move in

order to generate the stable density profile and the Thorpe scale L_T is defined as the root mean square of the Thorpe displacements:

$$L_T = \langle d^2(z) \rangle^{\frac{1}{2}}, \tag{7}$$

where $\langle\ \rangle$ is a vertical average. Itsweire (1984) found that in laboratory grid-generated turbulence the overturning lengthscale L_t defined by Ellison (1975) could be linearly related to the Thorpe scale L_T used in oceanic microstructure measurements as

$$L_T \approx 1.2 L_t \tag{8}$$

as long as the flow contains some overturning turbulent scales and the intensity of the internal-wave field remains small. Itsweire (1984) also showed that the largest overturns were equal to $2.74 L_T$ where the flow was turbulent. Therefore, in order to make comparisons with oceanic observations easier and avoid any arbitrary multiplier, we shall recast the inequalities of (5) in terms of the lengthscale L_t essentially equivalent to the Thorpe scale in the absence of internal waves (Caldwell 1983). Then, (5) yields

$$L_t = 0.7 L_O \quad \text{at the onset of buoyancy effects,} \tag{9a}$$

$$L_t = 7.8 L_K \quad \text{at the extinction of turbulence.} \tag{9b}$$

The *largest* overturns might be two to three times larger than L_t. $L_t = 0.7 L_O$ (from (9*a*)) is well correlated with the microstructure measurements by Dillon (1982) in the wind-forced mixing layer of a lake and the seasonal thermocline of the ocean, where

$$L_T \approx 0.8 L_O \tag{10}$$

except near the surface of the mixing layer where the buoyancy forces are thought to be small compared with the inertial forces.

3.2. *Vertical mixing and criterion for the extinction of turbulence*

As a criterion for the extinction of all overturning turbulent motions, SHV followed the ideas of Stewart (1969) based on the fact that for a linear internal-wavefield the vertical velocity and the density fluctuation are 90° out of phase, and thus the buoyancy flux $(g/\bar{\rho})\overline{\rho w}$ is zero and no vertical mixing takes place. The criterion $\overline{\rho w} \approx 0$ is rigorously true only for linear waves and may on average be valid for weakly nonlinear waves. It is therefore a sufficient but not a necessary condition for the extinction of turbulent motions. From the cospectra of ρ and w for R23 (SHV), Van Atta, Helland & Itsweire (1984, hereinafter referred to as VHI) found experimental evidence that some mixing was produced by scales for which the flow was no longer turbulent according to (5). These cospectra are shown in figure 2, replotted from VHI figure 5. If the cospectrum of ρ and w is a good indicator of the presence of turbulence, then the cospectrum shown in figure 2 should be significantly non-zero (above noise) for the wavenumbers lying between $1/0.7 L_O$ and $1/7.8 K_K$. These boundaries are shown in figure 2 as coupled sets of arrows delimiting the wavenumber domains that are consistent with the scale sizes considered turbulent by our earlier scale arguments. We see that at $x/M = 100$ the cospectrum is zero, consistent with our assumption that a vanishing $\overline{\rho w}$ means that no turbulence is present, a non-trivial result since a vanishing $\overline{\rho w}$ does not imply that the cospectrum must be identically zero at all wavenumbers. Note that VHI's figure 5 erronously included a factor of 2π in the definition of the wavenumbers. The region outside the wavenumber band may be a mixture of fossil turbulence and nonlinear internal waves.

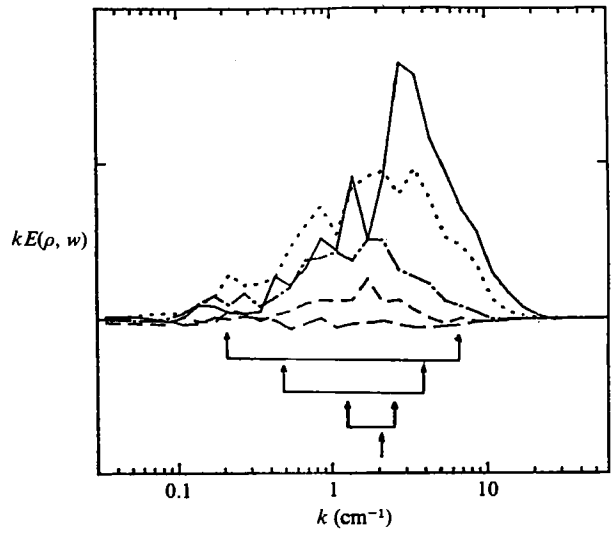

FIGURE 2. Cospectra of ρ and w for SHV's data ($N = 0.45$ rad/s) at various x/M. The coupled sets of arrows mark the range of scales that are believed to be turbulent according to (9). ——, $x/M = 10$; . . . , 20; · · · · · ·, 40; - - -, 60; —, 100.

At the x/M station where $\overline{\rho w} \approx 0$, we determined that the scale factor relating the Kolmogorov scale L_K to the smallest overturning scale of the flow was 7.8 ((9)). It is reasonable to assume that for any stratification the smallest turbulent scale is $7.8L_K$ or some constant times the Kolmogorov scale L_K, since the small scales will not feel the effects of buoyancy until the near-extinction of the turbulence. It is also reasonable to assume that the same scale would be the smallest possible scale contributing to the vertical mixing. The cospectrum data of figure 2 show that the wavenumber $1/7.8L_K$ is larger than the wavenumber of the peak of the cospectra of ρ and w (in area-preserving coordinates), but some of the buoyancy flux comes from contributions of wavenumbers greater than $1/7.8L_K$ (or equivalently from scales smaller than $7.8L_K$). In other words, scales affected by viscosity produce a substantial amount of turbulent mixing. The smallest lengthscale contributing to the vertical mixing, defined as the wavenumber at which the ρ, w cospectrum goes to zero, is 2.5 times L_K, which is approximately three times smaller than the $7.8L_K$ obtained from the $\overline{\rho w} \approx 0$ criterion.

4. Lengthscales and buoyancy-flux measurements

4.1. *Evolution of lengthscales and onset of buoyancy effects*

In order to compare the present data with SHV's results, the various lengthscales relevant to the dynamical evolution of the flow were computed. Two sets of data (R36 and R37) were taken with the large-M grid ($M = 3.81$ cm) and one set (R52) with the small-M grid ($M = 1.905$ cm) to complement the SHV data (R23). The relevant statistics and lengthscales for these three runs are summarized in table 2. In addition to these statistics, the mean density along the centreline of the test section was $\bar{\rho} = 1.012$ g/cm^3 and the average kinematic viscosity was $\nu = 0.009$ cm^2/s. Figure 3 shows the scalar (density) growth and decay for a number of stratifications. The solid

x/M	U (cm/s)	u' (cm/s)	w' (cm/s)	ρ' (g/cm^3)	$\frac{\overline{\rho w}}{\rho' w'}$	ϵ (cm^2/s^3)	$10^7\chi$ (g^2/cm^6/s)	N (s^{-1})	L_t (cm)	L_K (cm)	L_O (cm)	L_b (cm)
5	23.44	1.704	1.501	5.76×10^{-4}	0.339	8.472	1.830	0.981	0.58	0.018	2.998	1.53
10	24.65	1.018	0.886	9.14×10^{-4}	0.378	1.532	6.160	0.987	0.91	0.027	1.263	0.90
15	25.08	0.874	0.687	8.36×10^{-4}	0.116	0.468	3.332	0.981	0.85	0.037	0.705	0.70
20	25.42	0.584	0.402	7.88×10^{-4}	−0.011	0.211	1.963	0.977	0.80	0.045	0.476	0.41
25	25.54	0.563	0.406	6.41×10^{-4}	−0.101	0.127	1.297	0.949	0.69	0.051	0.385	0.43
30	25.75	0.512	0.362	5.44×10^{-4}	−0.055	0.074	0.846	0.904	0.64	0.058	0.316	0.40
40	26.06	0.426	0.371	4.21×10^{-4}	−0.064	0.042	0.501	0.853	0.56	0.067	0.260	0.43
50	26.48	0.518	0.368	3.21×10^{-4}	−0.123	0.024	0.180	0.799	0.49	0.077	0.216	0.46
60	26.92	0.376	0.249	2.97×10^{-4}	−0.013	0.018	0.084	0.803	0.44	0.082	0.187	0.31
70	27.61	0.440	0.223	3.20×10^{-4}	0.180	0.011	0.035	0.800	0.48	0.092	0.149	0.28
5	25.39	2.132	1.972	3.20×10^{-4}	0.175	8.654	0.633	0.658	0.71	0.017	5.505	2.99
10	25.94	1.072	0.979	3.54×10^{-4}	0.351	1.628	0.775	0.634	0.85	0.026	2.529	1.54
15	26.34	0.868	0.747	3.68×10^{-4}	0.374	0.536	0.740	0.608	0.97	0.035	1.542	1.23
20	26.57	0.622	0.540	3.67×10^{-4}	0.240	0.219	0.450	0.576	1.02	0.044	1.070	0.94
25	26.82	0.572	0.399	3.33×10^{-4}	0.195	0.114	0.418	0.568	1.00	0.051	0.791	0.70
30	26.99	0.516	0.340	3.19×10^{-4}	0.097	0.076	0.288	0.552	1.01	0.057	0.671	0.62
40	27.08	0.528	0.238	2.64×10^{-4}	−0.030	0.039	0.151	0.535	0.89	0.067	0.506	0.44
50	27.55	0.403	0.281	2.23×10^{-4}	−0.138	0.026	0.071	0.530	0.73	0.074	0.419	0.53
60	27.81	0.380	0.261	1.91×10^{-4}	−0.011	0.019	0.033	0.462	0.87	0.080	0.439	0.56
70	28.09	0.420	0.317	1.61×10^{-4}	−0.090	0.013	0.016	0.450	0.78	0.087	0.385	0.71
5	24.95	2.334	1.549	0.98×10^{-4}	0.296	9.034	0.096	0.348	0.78	0.017	14.621	4.45
10	25.65	1.289	0.967	1.03×10^{-4}	0.403	1.928	0.080	0.334	0.90	0.025	7.189	2.89
15	26.30	1.065	0.879	1.05×10^{-4}	0.443	0.610	0.094	0.319	1.00	0.033	4.330	2.75
20	26.54	0.803	0.649	0.99×10^{-4}	0.459	0.271	0.072	0.302	1.06	0.041	3.136	2.15
25	26.71	0.658	0.523	0.94×10^{-4}	0.464	0.151	0.049	0.280	1.17	0.047	2.630	1.87
30	26.70	0.488	0.353	0.74×10^{-4}	0.328	0.103	0.042	0.248	1.18	0.052	2.602	1.43
40	26.98	0.529	0.399	0.83×10^{-4}	0.400	0.043	0.022	0.241	1.38	0.065	1.742	1.65
50	27.36	0.508	0.310	0.80×10^{-4}	0.377	0.029	0.015	0.227	1.50	0.071	1.561	1.37
60	26.97	0.922	0.271	0.78×10^{-4}	0.327	0.021	0.008	0.215	1.63	0.077	1.442	1.26
70	27.88	0.455	0.241	0.68×10^{-4}	0.118	0.017	0.004	0.206	1.56	0.081	1.392	1.17
80	28.29	0.427	0.226	0.62×10^{-4}	0.090	0.012	0.002	0.198	1.52	0.088	1.258	1.14

TABLE 2(a). Turbulence statistics and lengthscales for a stratified flow; uniform velocity profile; R36 (grid mesh size $M = 3.81$ cm); $\bar{\rho} = 1.012$ g/cm^3

x/M	U (cm/s)	u' (cm/s)	w' (cm/s)	ρ' (g/cm^3)	$\frac{\overline{\rho w}}{\rho' w'}$	ϵ (cm^2/s^3)	$10^7\chi$ (g^2/cm^6/s)	N (s^{-1})	L_t (cm)	L_K (cm)	L_O (cm)	L_b (cm)
5	25.20	2.133	1.979	7.65×10^{-4}	0.306	10.632	7.300	1.026	0.71	0.017	3.137	1.93
10	25.17	1.224	1.017	8.71×10^{-4}	0.332	1.947	6.420	1.023	0.80	0.026	1.349	0.99
15	25.46	0.868	0.632	8.17×10^{-4}	0.187	0.600	3.840	1.016	0.76	0.035	0.756	0.62
20	25.83	0.671	0.476	7.14×10^{-4}	0.056	0.276	2.430	1.022	0.66	0.043	0.509	0.47
25	26.10	0.553	0.451	6.23×10^{-4}	−0.025	0.172	1.780	0.978	0.63	0.048	0.429	0.46
30	26.36	0.515	0.398	5.56×10^{-4}	−0.033	0.115	1.182	0.972	0.57	0.053	0.354	0.41
40	26.35	0.423	0.332	4.71×10^{-4}	0.046	0.048	0.643	0.960	0.50	0.066	0.234	0.35
50	26.39	0.419	0.298	3.85×10^{-4}	−0.023	0.033	0.261	0.934	0.43	0.073	0.201	0.32
60	26.34	0.408	0.307	3.28×10^{-4}	0.016	0.024	0.144	0.908	0.38	0.078	0.180	0.34
5	25.37	2.185	1.947	5.15×10^{-4}	0.284	10.584	2.980	0.820	0.74	0.017	4.381	2.37
10	25.00	1.213	1.036	5.62×10^{-4}	0.356	2.047	2.360	0.817	0.81	0.026	1.939	1.27
15	25.51	0.856	0.678	5.71×10^{-4}	0.317	0.620	2.080	0.794	0.88	0.035	1.114	0.85
20	25.68	0.688	0.491	5.23×10^{-4}	0.233	0.263	1.520	0.775	0.84	0.043	0.752	0.63
25	25.75	0.582	0.397	4.70×10^{-4}	0.066	0.155	0.905	0.751	0.81	0.049	0.606	0.53
30	25.87	0.504	0.367	4.16×10^{-4}	0.060	0.104	0.608	0.740	0.73	0.054	0.506	0.50
40	26.03	0.429	0.342	3.46×10^{-4}	0.095	0.048	0.313	0.723	0.65	0.065	0.357	0.47
50	26.23	0.384	0.277	2.98×10^{-4}	−0.022	0.031	0.147	0.666	0.65	0.073	0.322	0.42
60	26.31	0.384	0.272	2.68×10^{-4}	−0.046	0.023	0.082	0.666	0.59	0.079	0.279	0.41
70	26.42	0.342	0.290	2.45×10^{-4}	−0.026	0.018	0.037	0.660	0.54	0.084	0.247	0.44
5	25.95	2.239	2.017	2.18×10^{-4}	0.239	10.625	0.492	0.530	0.75	0.017	8.451	3.81
10	25.53	1.269	1.110	2.31×10^{-4}	0.353	2.178	0.485	0.505	0.88	0.025	4.116	2.20
15	25.82	0.867	0.731	2.21×10^{-4}	0.353	0.653	0.311	0.475	0.95	0.034	2.468	1.54
20	26.05	0.702	0.550	2.17×10^{-4}	0.351	0.303	0.226	0.463	0.99	0.041	1.749	1.19
30	26.57	0.541	0.370	2.00×10^{-4}	0.214	0.109	0.142	0.444	0.98	0.053	1.117	0.83
40	26.84	0.482	0.307	1.86×10^{-4}	0.078	0.051	0.081	0.443	0.92	0.064	0.764	0.69
50	26.85	0.411	0.282	1.61×10^{-4}	0.012	0.038	0.049	0.427	0.85	0.069	0.695	0.66
60	27.42	0.394	0.283	1.46×10^{-4}	0.064	0.025	0.029	0.417	0.82	0.076	0.584	0.68
70	27.71	0.336	0.286	1.31×10^{-4}	0.110	0.021	0.016	0.370	0.92	0.079	0.647	0.77
80	27.97	0.359	0.274	1.10×10^{-4}	0.079	0.016	0.010	0.355	0.84	0.085	0.595	0.77

5	25.55	2.250	2.023	0.59×10^{-4}	0.245	11.051	0.046	0.291	0.72	0.016	21.130	6.94
10	25.08	1.224	1.144	0.68×10^{-4}	0.369	2.255	0.039	0.283	0.83	0.024	9.993	4.05
20	25.55	0.700	0.614	0.74×10^{-4}	0.451	0.332	0.028	0.258	1.07	0.040	4.387	2.38
30	26.09	0.532	0.446	0.82×10^{-4}	0.455	0.111	0.022	0.256	1.22	0.052	2.573	1.74
40	23.94	0.477	0.327	0.66×10^{-4}	0.368	0.063	0.018	0.231	1.20	0.060	2.262	1.42
50	24.13	0.402	0.320	0.63×10^{-4}	0.314	0.045	0.012	0.230	1.15	0.065	1.916	1.39
60	26.81	0.462	0.352	0.55×10^{-4}	0.352	0.034	0.010	0.205	1.28	0.070	1.989	1.72
70	27.71	0.214	0.145	0.40×10^{-4}	0.116	0.012	0.007	0.190	1.02	0.091	1.308	0.76

TABLE 2(*b*). Turbulence statistics and lengthscales for a stratified flow; uniform velocity profile; R37 (grid mesh size $M = 3.81$ cm); $\bar{\rho} = 1.012$ g/cm^3

x/M	U (cm/s)	u' (cm/s)	w' (cm/s)	ρ' (g/cm^3)	$\overline{\rho w}/\rho' w'$	ϵ (cm^2/s^3)	$10^7\chi$ (g^2/cm^6/s)	N (s^{-1})	L_t (cm)	L_K (cm)	L_O (cm)	L_b (cm)
5	25.00	1.974	1.539	4.70×10^{-4}	0.197	9.718	2.300	0.936	0.52	0.017	3.440	1.64
10	24.30	1.227	0.918	4.76×10^{-4}	0.282	2.559	1.800	0.936	0.53	0.023	1.768	0.98
15	24.27	0.880	0.723	5.07×10^{-4}	0.322	0.913	1.470	0.928	0.57	0.030	1.069	0.78
20	24.57	0.897	0.737	5.34×10^{-4}	0.182	0.406	1.250	0.926	0.60	0.037	0.715	0.80
30	24.52	0.592	0.414	5.45×10^{-4}	0.061	0.147	0.050	0.949	0.58	0.048	0.415	0.44
40	24.71	0.613	0.447	4.68×10^{-4}	−0.036	0.087	0.678	0.939	0.51	0.054	0.324	0.48
50	25.08	0.564	0.486	4.06×10^{-4}	−0.008	0.064	0.499	0.944	0.44	0.059	0.276	0.52
60	25.45	0.822	0.679	3.61×10^{-4}	0.039	0.052	0.355	0.926	0.40	0.062	0.256	0.73
80	25.52	0.595	0.404	2.98×10^{-4}	0.002	0.021	0.180	0.908	0.35	0.077	0.167	0.45
100	25.55	0.444	0.381	2.72×10^{-4}	−0.048	0.016	0.100	0.907	0.32	0.083	0.146	0.42
5	26.89	2.117	1.662	3.90×10^{-4}	0.233	9.561	1.950	0.841	0.53	0.017	4.008	1.98
10	26.25	1.320	0.976	3.61×10^{-4}	0.288	2.442	1.150	0.808	0.54	0.023	2.152	1.21
15	25.89	0.938	0.726	3.72×10^{-4}	0.322	0.918	0.914	0.783	0.59	0.030	1.384	0.93
20	25.74	0.776	0.609	3.79×10^{-4}	0.296	0.434	0.814	0.760	0.63	0.036	0.995	0.80
25	25.86	0.698	0.496	3.67×10^{-4}	0.221	0.237	0.694	0.717	0.69	0.042	0.802	0.69
30	26.34	0.435	0.610	3.50×10^{-4}	−0.112	0.153	0.580	0.713	0.67	0.047	0.651	0.86
40	26.59	0.647	0.618	3.20×10^{-4}	0.054	0.086	0.476	0.705	0.62	0.054	0.494	0.88
50	26.52	0.561	0.362	3.00×10^{-4}	−0.063	0.053	0.330	0.705	0.58	0.060	0.390	0.51
60	26.59	0.567	0.473	2.72×10^{-4}	0.011	0.047	0.256	0.694	0.54	0.062	0.373	0.68
70	27.07	0.610	0.492	2.41×10^{-4}	0.053	0.078	0.195	0.674	0.51	0.055	0.506	0.73
90	26.42	0.514	0.326	2.08×10^{-4}	0.067	0.021	0.098	0.674	0.44	0.076	0.259	0.48
110	25.94	0.389	0.238	1.87×10^{-4}	0.032	0.014	0.057	0.673	0.40	0.084	0.212	0.35

TABLE 2(*c*). Continued on next page

x/M	U (cm/s)	u' (cm/s)	w' (cm/s)	ρ' (g/cm^3)	$\overline{\rho w}/\overline{\rho' w'}$	ϵ (cm^2/s^3)	$10^7\chi$ (g^2/cm^6/s)	N (s^{-1})	L_t (cm)	L_K (cm)	L_O (cm)	L_b (cm)
5	26.84	2.168	1.628	1.95×10^{-4}	0.210	9.298	1.210	0.587	0.55	0.017	6.773	2.77
10	26.10	1.269	1.019	1.80×10^{-4}	0.298	2.607	0.310	0.567	0.54	0.023	3.779	1.80
15	25.81	0.928	0.696	1.83×10^{-4}	0.387	0.951	0.249	0.544	0.60	0.029	2.433	1.28
20	25.81	0.765	0.572	1.85×10^{-4}	0.358	0.483	0.215	0.531	0.63	0.034	1.799	1.08
25	26.10	0.726	0.575	1.92×10^{-4}	0.247	0.276	0.208	0.518	0.69	0.040	1.407	1.11
30	25.80	0.562	0.392	1.79×10^{-4}	0.336	0.176	0.192	0.488	0.82	0.044	1.231	0.80
40	25.70	0.563	0.379	1.72×10^{-4}	0.235	0.091	0.131	0.469	0.77	0.052	0.936	0.81
50	25.58	0.488	0.382	1.72×10^{-4}	0.160	0.064	0.107	0.469	0.76	0.057	0.785	0.81
60	25.43	0.432	0.282	1.64×10^{-4}	0.132	0.050	0.084	0.469	0.72	0.060	0.698	0.60
80	25.80	0.462	0.219	1.46×10^{-4}	0.065	0.027	0.061	0.468	0.64	0.071	0.508	0.47
100	25.91	0.495	0.332	1.39×10^{-4}	0.085	0.024	0.031	0.468	0.61	0.073	0.481	0.71
120	25.14	0.458	0.318	1.96×10^{-4}	0.095	0.018	0.022	0.468	0.87	0.078	0.416	0.68
5	25.39	2.009	1.502	0.93×10^{-4}	0.245	9.420	0.093	0.416	0.52	0.016	11.452	3.61
10	24.76	1.212	0.939	0.86×10^{-4}	0.282	2.544	0.046	0.393	0.54	0.022	6.477	2.39
20	24.60	0.735	0.537	0.99×10^{-4}	0.328	0.475	0.035	0.384	0.65	0.034	2.898	1.40
40	24.77	0.556	0.450	1.10×10^{-4}	0.201	0.096	0.023	0.364	0.80	0.051	1.408	1.24
60	24.98	0.423	0.254	1.08×10^{-4}	0.249	0.044	0.016	0.336	0.92	0.062	1.073	0.75
80	25.19	0.366	0.297	1.10×10^{-4}	0.067	0.022	0.012	0.340	0.92	0.073	0.745	0.87
100	25.14	0.343	0.185	1.00×10^{-4}	0.035	0.017	0.008	0.347	0.81	0.078	0.639	0.53
120	26.65	0.415	0.267	0.93×10^{-4}	0.056	0.022	0.006	0.346	0.75	0.073	0.733	0.77

TABLE 2(*c*). Turbulence statistics and lengthscales for a stratified flow; uniform velocity profile; R52 (grid mesh size $M = 1.905$ cm); $\bar{\rho} = 1.012$ g/cm^3

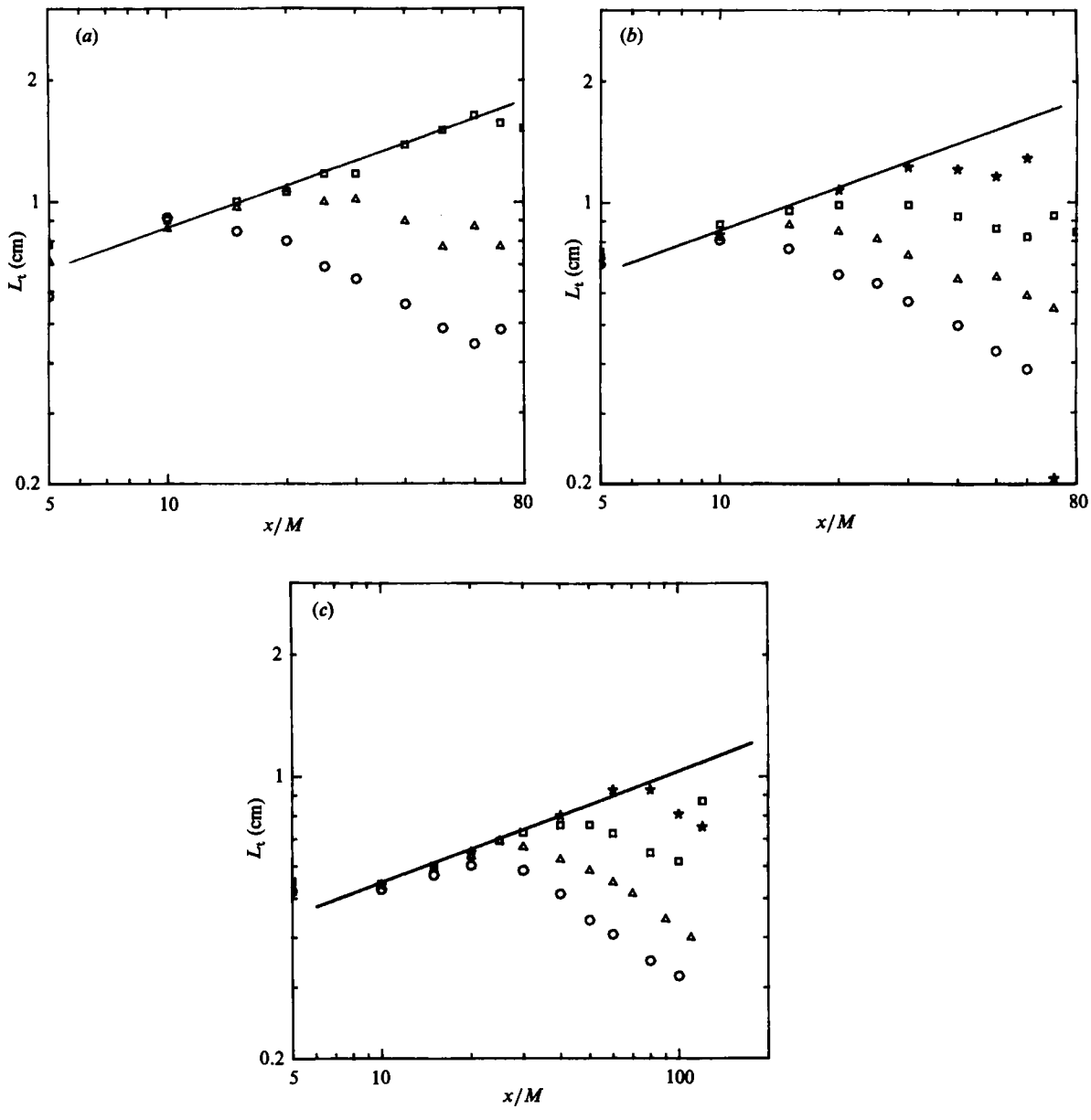

FIGURE 3. Overturning turbulent lengthscale L_t *vs.* downstream distance from the grid x/M. (*a*) R36 ($M = 3.81$ cm): ○, $N = 0.90$ rad/s; △, 0.56; □, 0.27. (*b*) R37 ($M = 3.81$ cm): ○, $N = 0.98$ rad/s; △, 0.74; □, 0.44; ★, 0.24. (*c*) R52 ($M = 1.905$ cm): ○, $N = 0.93$ rad/s: △, 0.73: □, 0.50: ★, 0.37.

line represents the growth rate of a passive scalar (Montgomery 1974). Table 3 summarizes the initial lengthscales (at $x/M = 10$) for SHV's data (R23) and the present measurements. For R36 and R37, at $x/M = 10$, the overturning lengthscale L_t is approximately equal to 0.85 cm compared with a value of 0.58 cm for SHV, indicating that doubling the grid mesh size produces an increase of roughly $\sqrt{2}$ in the overturning scale L_t.

Reference	N (s^{-1})	M (cm)	L_O (cm)	L_t (cm)	$\frac{L_O}{M}$	$\frac{L_O}{L_t}$
R23	0.95	1.905	2.66	0.59	1.40	4.50
(SHV)	0.73	1.905	3.64	0.57	1.91	6.38
	0.45	1.905	7.16	0.56	3.76	12.68
R52	0.93	1.905	1.77	0.52	0.93	3.38
	0.73	1.905	2.15	0.53	1.13	4.02
	0.50	1.905	3.78	0.54	1.98	7.00
	0.37	1.905	6.48	0.54	3.40	12.00
R36	0.90	3.81	0.63	0.82	0.33	1.38
	0.55	3.81	2.53	0.85	0.66	2.96
	0.36	3.81	7.19	0.90	1.89	7.98
R37	0.97	3.81	1.35	0.80	0.35	1.68
	0.74	3.81	1.94	0.81	0.51	2.38
	0.43	3.81	4.12	0.88	1.08	4.68
	0.24	3.81	9.99	0.83	2.62	12.04

TABLE 3. Initial Ozmidov and turbulent lengthscale ratios for SHV's data and the present experiments at $x/M = 10$

Reference	x/M	Nt	L_t (cm)	L_O (cm)	$\frac{L_t}{L_O}$	ϵ_0 (cm^2/s^3)	DCo_0N^2 (cm^2/s^3)
R23	22	1.74	0.635	0.80	0.795	0.650	0.081
(SHV)	30	1.71	0.755	0.88	0.970	0.245	0.043
	40	1.41	0.840	1.07	0.785	0.116	0.021
R52	20	1.44	0.600	0.72	0.840	0.406	0.068
	25	1.33	0.690	0.80	0.860	0.237	0.065
	45	1.57	0.770	0.83	0.930	0.077	0.024
	60	1.54	0.925	1.07	0.860	0.044	0.007
R36	12	1.82	0.910	1.10	0.825	1.080	0.218
	18	1.49	1.025	1.20	0.895	0.390	0.086
R37	12	1.90	0.845	1.05	0.805	1.520	0.224
	15	1.78	0.950	1.11	0.855	0.620	0.146
	25	1.63	1.070	1.43	0.750	0.190	0.037

TABLE 4. Onset of buoyancy effects (beginning of fossilization) according to (9*a*) for SHV's data (1983) and the present experiments

The critical ratio between the Ozmidov scale L_O and the vertical turbulent scale L_t at the onset of buoyancy effects (departure from passive-scalar growth) are presented in table 4. The average ratio is:

$$L_t = (0.85 \pm 0.06)\, L_O \tag{11}$$

compared to the value of $0.7L_O$ proposed by SHV. There is no observable effect of the grid mesh on this ratio. The present ratio given in (11) is thought to be more accurate than the earlier estimate of SHV.

The effect of the increased grid mesh size M on the Ozmidov and buoyancy scales

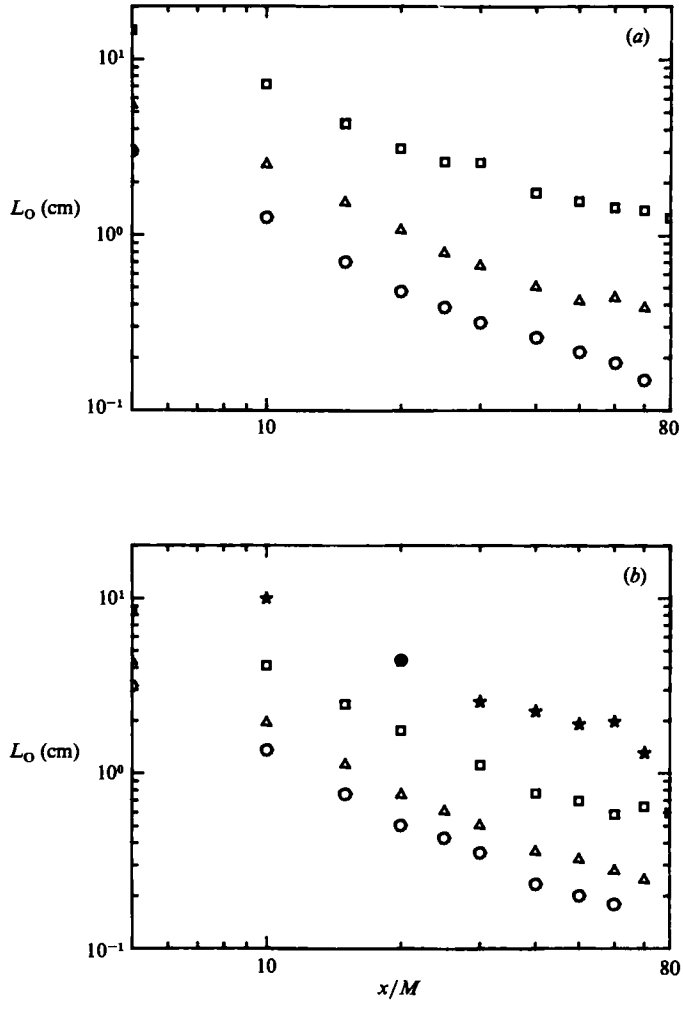

FIGURE 4. Ozmidov lengthscale L_O *vs* downstream distance from the grid x/M; $M = 3.81$ cm. (*a*) R36: ○, $N = 0.90$ rad/s; △, 0.56; □, 0.27. (*b*) R37: ○, $N = 0.98$ rad/s; △, 0.74; □, 0.44; ★, 0.24.

may be seen in figures 4 and 5 respectively. Both lengthscales decrease monotonically away from the grid as the turbulence decays. The general behaviour of the two lengthscales is very similar in nature except for the stations farthest from the grid where L_b decreases at a slower rate than L_O, since, as SHV noted, L_b includes contributions from internal waves whereas L_O depends mostly on the smaller scales contributing to the dissipation rate.

Figure 6 compares the two *buoyancy* lengthscales for R36 and R37. A least-square fit through the data in the region where the internal-wave contributions to L_b are thought to be negligible (large values of L_O and L_b corresponding to the smallest values of x/M) yields the following relationship:

$$L_O = 1.31(L_b)^{1.4}. \tag{12}$$

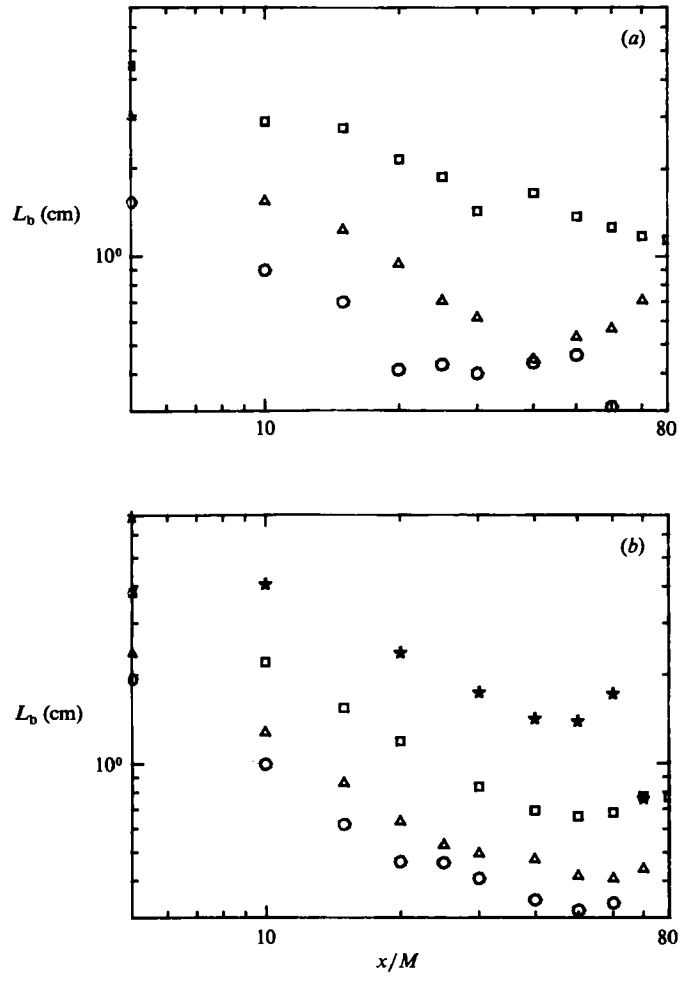

FIGURE 5. Buoyancy lengthscale L_b *vs.* downstream distance from the grid x/M; $M = 3.81$ cm. (*a*) R36: ○, $N = 0.90$ rad/s; △, 0.56; □, 0.27. (*b*) R37: ○, $N = 0.98$ rad/s; △, 0.74; □, 0.44; ★, 0.24.

The data for the lightest stratification of R37 (□ in figure 6) were not included in the fit because of the uncertainty in measuring the mean density gradient. Equation (12) can be compared with

$$L_O = 1.49(L_b)^{1.53} \tag{13}$$

obtained for SHV's data and R52 (figure 7). If the turbulence were isotropic and the dissipation rate of turbulent kinetic energy could be expressed as $\epsilon = (\overline{w^2})^{\frac{3}{2}}/l$, with $l = L_b \equiv L_O$, then the Ozmidov and buoyancy lengthscales would be equal. In the present experiments the vertical velocity fluctuation w' is always smaller than the horizontal-velocity fluctuation u' and even decays at a faster rate for R36 and R37, as shown in §5.1.

For the towed-grid experiments of Lin & Veenhuizen (1975) in which both the dissipation rate ϵ and the vertical-velocity fluctuation w' were measured

$$\overline{w^2} \propto \left(\frac{x}{M}\right)^{-1.65}, \quad \epsilon \propto \left(\frac{x}{M}\right)^{-2.3}, \tag{14}$$

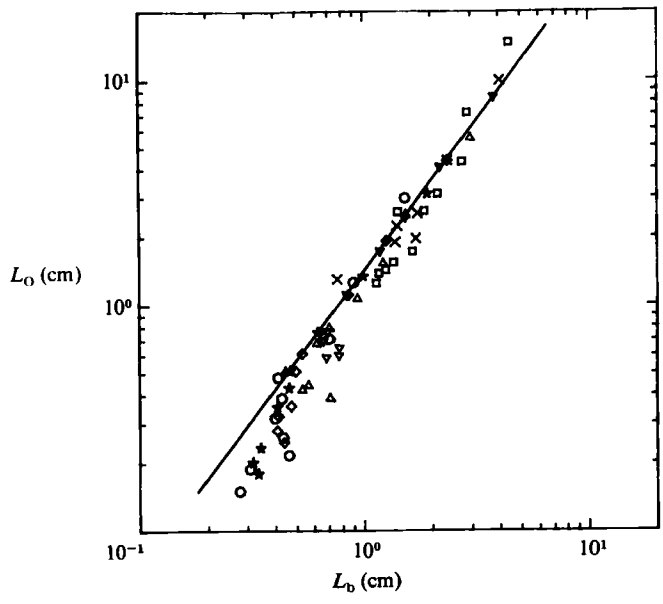

FIGURE 6. Ozmidov scale L_O *vs.* buoyancy scale L_b for various stratifications; $M = 3.81$ cm; R36 and R37.

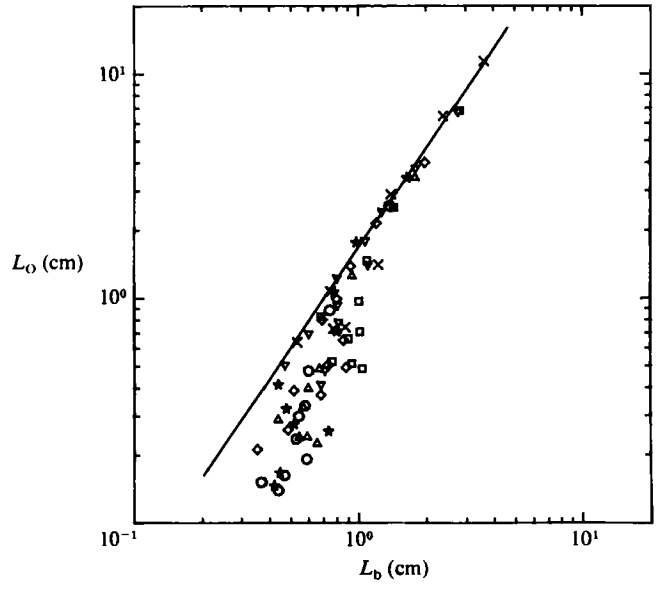

FIGURE 7. Ozmidov scale L_O *vs* buoyancy scale L_b for various stratifications; $M = 1.905$ cm; R23 (SHV 1983) and R52.

which can be expressed in terms of L_O and L_b as

$$L_O \propto L_b^{1.39} N^{0.11}, \tag{15}$$

in good agreement with (12) and (13) considering the difference in Reynolds numbers, grid geometries, and towed *versus* not-towed experimental techniques. The weak dependence on the Brunt–Väisälä frequency can be neglected for the range of

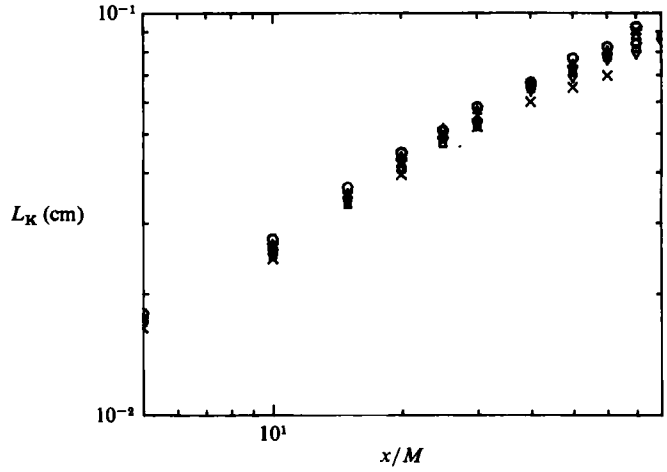

FIGURE 8. Kolmogorov lengthscale L_K *vs.* downstream distance from the grid x/M for various stratifications; $M = 3.81$ cm; R36 and R37.

stratifications investigated. Lin & Veenhuizen (1975) did not report any departures from these power laws, which is consistent with the low level of internal waves achievable in their tow tank. The data of figure 6 for our large-M grid are close to the solid line defined by (12), even when buoyancy effects dominate the turbulence. Such is not the case for the small-M grid data of figure 7 and especially the three decays of R23 (SHV), where substantial departures from (13) are observed far from the grid. These deviations from the limiting wholly turbulent case (no initial wavefield) provide some evidence that, for R23 and R52, a substantial internal wavefield is present near the grid. This wavefield will eventually dominate the velocity fluctuations as the turbulence decays (see §§ 5.2 and 5.3).

The evolution of the Kolmogorov scale L_K (figure 8) is virtually independent of the stratification since the dissipation rate ϵ comes from the small turbulent scales of the flow, which are the last ones to feel the buoyancy effects. As one moves farther away from the grid the kinetic-energy dissipation rate decreases and so does the Kolmogorov scale L_K.

4.2. *Buoyancy flux and extinction of turbulence*

The buoyancy flux $(g/\bar{\rho})\ \overline{\rho w}$ is an important parameter for measuring the amount of turbulent mixing occurring at any location in the flow (Rohr *et al.* 1984) and can be used as a criterion for the extinction of turbulence as mentioned previously. Figure 9 shows the evolution of the normalized buoyancy flux $\overline{\rho w}/\rho' w'$ as a function of the distance from the grid x/M for several stratifications. Measurements taken close to the grid show that $\overline{\rho w}/\rho' w'$ appears to grow from zero at the grid (corresponding to uncorrelated density and velocity fields) to a maximum value of 0.4. This asymptotic value is the same as the one measured by Tavoularis & Corrsin (1981) in a weakly stratified (passive scalar from a dynamical point of view) homogeneous shear flow. However, the passive-scalar (small temperature gradient in air) grid experiment of Sirivat & Warhaft (1983) produced an asymptotic value of 0.7 for the normalized correlation between temperature and vertical velocity. This asymptotic passive value is never closely approached even for the lightest

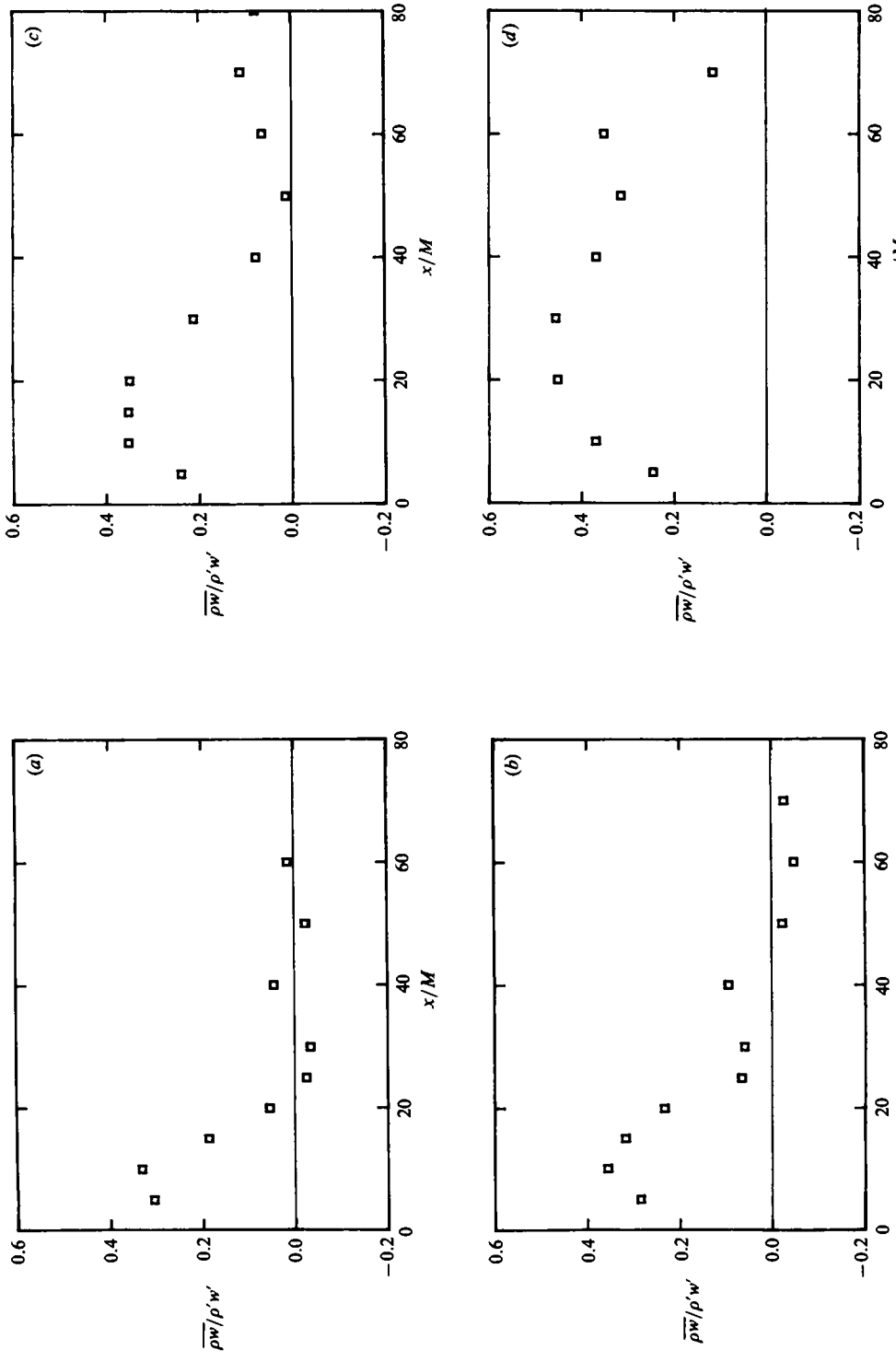

FIGURE 9. Normalized buoyancy flux $\overline{\rho w}/\rho' w'$ *vs* downstream distance from the grid x/M; R37 (M = 3.81 cm); (*a*) N = 0.98 rad/s; (*b*) 0.74; (*c*) 0.44; (*d*) 0.24.

Reference	x/M	Nt	L_O (cm)	L_K (cm)	$\frac{L_O}{L_K}$	ϵ_{tr} (cm^2/s^3)	$DCo_{tr}N^2$ (cm^2/s^3)
R23	38	3.00	0.40	0.051	7.55	0.143	0.040
(SHV)	50	2.78	0.43	0.059	7.32	0.073	0.022
	78	2.60	0.64	0.076	8.42	0.035	0.013
R52	35	2.55	0.37	0.051	7.25	0.110	0.042
	45	2.28	0.44	0.057	7.75	0.068	0.036
	80	2.77	0.51	0.071	7.16	0.027	0.013
	120	2.97	0.58	0.073	7.95	0.022	0.004
R36	20	2.93	0.48	0.045	10.60	0.211	0.096
	35	2.67	0.59	0.062	9.50	0.054	0.031
R37	22	3.26	0.44	0.045	9.71	0.200	0.082
	30	3.27	0.51	0.054	9.44	0.115	0.049
	50	3.03	0.69	0.069	10.07	0.038	0.012

TABLE 5. Extinction of turbulence (complete fossilization) according to (9*b*) for SHV's data (1983) and the present experiments

stratification of R37 where buoyancy effects are smallest in our data. This result suggests a rather strong dependance of $\overline{\rho w}/\rho' w'$ on N for small values of N.

The relevant parameters and lengthscales at that point in the flow where $\overline{\rho w}$ first approaches zero (corresponding to the extinction of turbulence or complete fossilization) are given in table 5. The ratio between the Ozmidov and the Kolmogorov scales appears to depend on the grid mesh size M. For the small mesh ($M = 1.905$ cm, SHV and R52) grid, we have:

$$L_O = (7.63 \pm 0.45)\, L_K, \tag{16}$$

and for the large mesh ($M = 3.81$ cm, R36 and R37) grid:

$$L_O = (9.86 \pm 0.48)\, L_K. \tag{17}$$

For either grid mesh size M, the experimental scatter in the L_O/L_K ratio is less than the difference between the averaged ratios for the two grid mesh sizes.

A careful re-examination of SHV's data (R23) with a lower threshold level on $\overline{\rho w}$ than used by them yields a value of 7.63 (16) for the ratio between Ozmidov and Kolmogorov scales at $\overline{\rho w} \approx 0$, lower than SHV's value of 11. From (16) and (17) and the definition of the Ozmidov and Kolmogorov lengthscales, the values of the transition dissipation rate ϵ_{tr} below which no overturning motion can be sustained are, respectively,

$$\epsilon_{tr} = (15 \pm 1.2)\, \nu N^2 \quad \text{for } M = 1.905 \text{ cm} \tag{18}$$

and

$$\epsilon_{tr} = (21 \pm 1.4)\, \nu N^2 \quad \text{for } M = 3.81 \text{ cm}. \tag{19}$$

The earlier estimate of SHV was $\epsilon_{tr} = 24.5 \nu N^2$. Preliminary centreline measurements in the wake behind a sphere (Itsweire, private communication) show a transition rate $\epsilon_{tr} = 29 \nu N^2$, in good agreement with Gibson's (1980) prediction of $\epsilon_{tr} = 30 \nu N^2$ for a turbulent patch near complete fossilization. These observations suggest that ϵ_{tr} might depend on the turbulence-generating mechanism (a single turbulent patch *versus* a spatially homogeneous turbulence). In addition (18) and (19) would suggest a slight increase of ϵ_{tr} with grid Reynolds number.

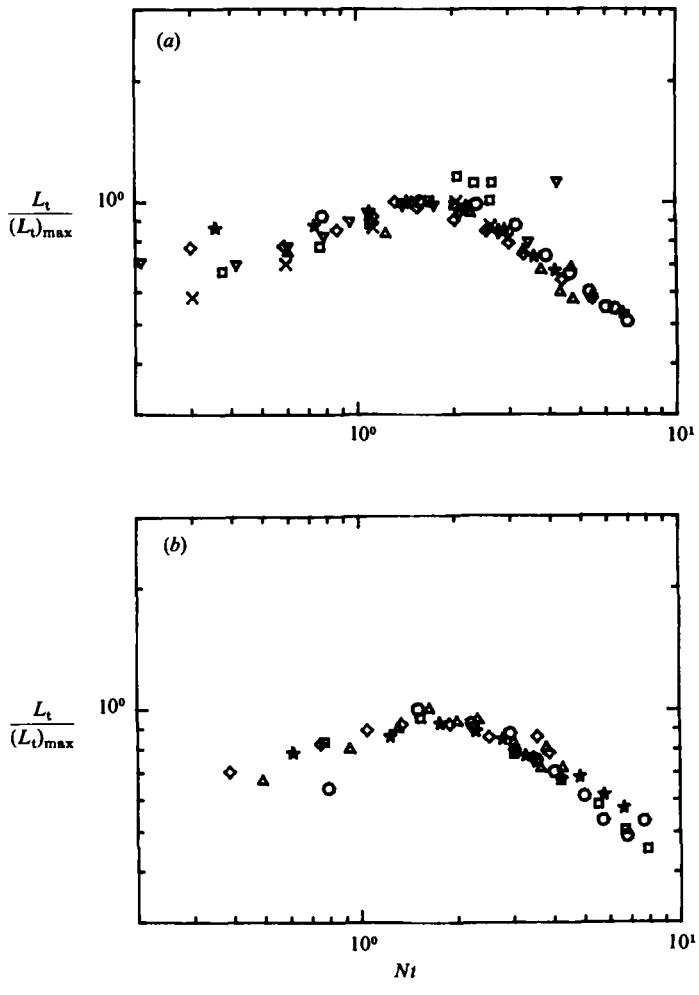

FIGURE 10. Overturning turbulent scale L_t normalized by its maximum at the onset of buoyancy effects (see table 3) for various stratifications *vs* non-dimensional time Nt. (*a*) $M = 1.905$ cm, R23 (SHV 1983) and R52. (*b*) $M = 3.81$ cm, R36 and R37.

4.3. *Transition time and final decay of fossil turbulence*

The evolution of the density fluctuations is replotted in figure 10 *versus* a non-dimensional time $Nt = (x/M)F_r^{-1}$, where $F_r = U/NM$ is an overall Froude number. The onset of buoyancy effects (departure from passive-scalar growth) occurred at an average value of $Nt \approx 1.7$ (see table 4) for the larger grid (R36 and R37) and at $Nt \approx 1.5$ for the smaller grid (SHV and R52). Since the initial dissipation rate ϵ and the turbulent scale L_t are nearly constant for a given grid mesh size M, and $L_t \propto M^{\frac{1}{2}}$, the onset time is roughly proportional to the initial ratio of $L_O/L_t = (\epsilon/(N^3M))^{\frac{1}{2}}$. Obviously, if initially $L_t \geqslant L_O$, the turbulence is always buoyancy dominated at the large scales and the transition time is 0 (as in Lin & Veenhuizen 1975 and Britter *et al.* 1983). From the plot of the normalized correlation between ρ and w *versus* dimensionless time in figure 11 we find that the extinction of turbulence or complete fossilization ($\overline{\rho w} \approx 0$) occurs at about $Nt = 3.03$ for the large-M grid (see table 5). In other words, all three-dimensional turbulence is suppressed in less than a quarter of

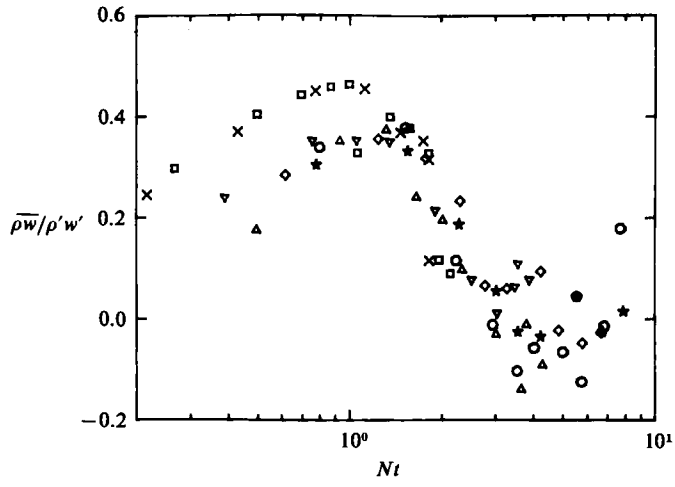

FIGURE 11. Normalized buoyancy flux $\overline{\rho w}/\rho' w'$ *vs* non-dimensional time Nt for various stratifications. $M = 3.81$ cm, R36 and R37.

a Brunt–Väisälä period after the initial onset of buoyancy effects. This time can be computed from the differences between the values of Nt given in tables 4 and 5 for any stratification N and grid mesh size M. After the onset of buoyancy effects the root-mean-square density fluctuation decays like $x^{-0.75}$ for $M = 1.905$ cm and like $x^{-0.64}$ for $M = 3.81$ cm. Lin & Veenhuizen (1975) found that the r.m.s. density fluctuation in their towed-grid experiment decayed like $x^{-0.75}$. Those rates are substantially slower than the t^{-1} decay rate predicted by the theory of two-dimensional turbulence (e.g. Lesieur & Herring 1984) assuming the density to be a passive scalar. In the present investigation the total density fluctuation is never a passive scalar since some small-scale fossil turbulence as well as internal waves are still present after $\overline{\rho w} \approx 0$. To compare the present data with passive-scalar two-dimensional-turbulence theory one would need to subtract the internal-wave contribution to $\rho(x, t)$. This is not possible for purely Eulerian data measured at a fixed location x. However, Itsweire (1984) reported that the Thorpe scale L_T, which is computed from measured vertical density displacements and is free of internal-wave contributions, decays as $x^{-1.05}$ after the extinction of three-dimensional turbulence according to the $\overline{\rho w} \approx 0$ criterion. This result indicates that, in the absence of internal-wave contributions, the turbulent part of the Eulerian density fluctuation could decrease at a rate close to the one predicted by the two-dimensional turbulence theory.

5. Turbulent velocity decay

5.1. *Experimental results*

Van Atta *et al.* (1983) pointed out that the available velocity fluctuation measurements in the flow of a linearly stratified fluid past a biplane grid or an array of vertical rods lead to widely different conclusions regarding the influence of stable stratification on the behaviour of the velocity fluctuations. The measurements to date can be qualitatively separated into two classes of behaviour whose occurrence is sensitive to the initial conditions of the flow as well as the type of facility, grid geometry and instrumentation technique used for the collection of data. The distinguishing

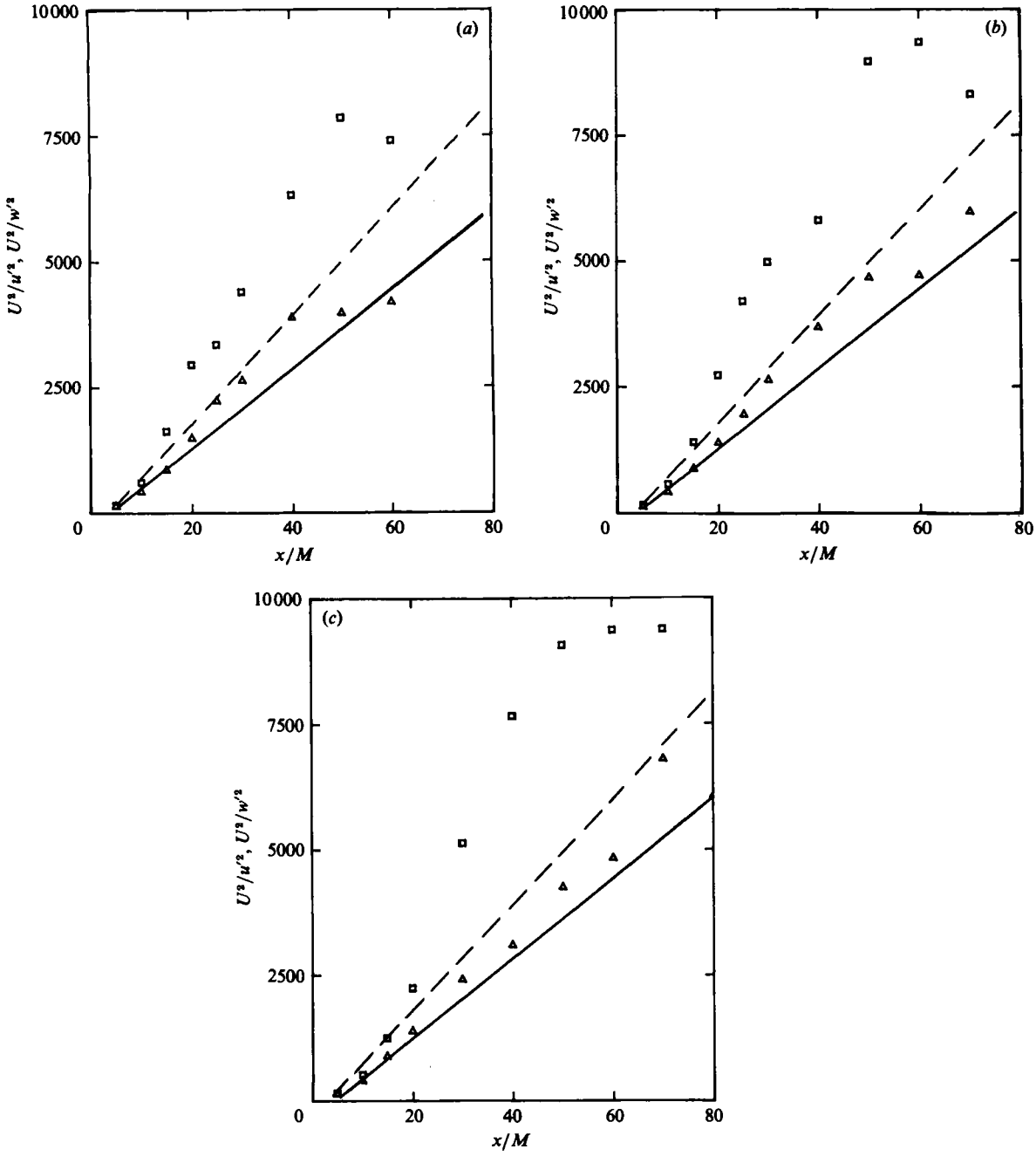

FIGURE 12. Inverse turbulent velocity intensities *vs.* downstream distance from the grid; R37, $M = 3.81$ cm; △, U^2/u'^2; □, $U^2/\overline{w^2}$: (*a*) $N = 0.98$ rad/s; (*b*) 0.74; (*c*) 0.44.

parameter is the intensity of internal waves present when the turbulence is generated by the grid.

Data in the first class (Lin & Veenhuizen 1975; Britter *et al.* 1983; and the present data of R36 and R37) are relatively free from internal waves near the grid. These measurements show that, as the turbulence feels the effects of buoyancy, the vertical

velocity decays at a faster rate than in the neutral case, while the horizontal components are basically unaffected and follow the usual Batchelor–Townsend (1948) decay. Such a behaviour is in agreement with intuition and visual observation in the laboratory (Lin & Pao 1974). One would expect that as buoyancy forces inhibit vertical motions they will also reduce vertical velocity fluctuations. Then, farther away from the grid or body, where three-dimensional turbulence has disappeared, one might expect an almost constant level of fluctuations as internal waves and fossil turbulence dissipate relatively little energy. Figure 12 illustrates this evolution of the longitudinal and vertical velocity fluctuations for the large-M grid (R37) which can be compared with the small-M grid data of SHV (their figures 5–7). Again the solid and dashed lines are least-square fits through unstratified grid data for u' and w', respectively.

Data in the second class have stronger internal wavefields near the grid and include those made by dropping a grid in a vertical tank (Dickey & Mellor 1980) and some UCSD data (SHV and R52). For the Dickey & Mellor experiments, it is difficult to estimate the level of internal waves generated by their grid as it plunged vertically down through a fluid of increasing density, since no direct comparisons have been made between towing a grid along a direction normal to the density gradient and dropping a grid along the direction of the density gradient. Intuitively, it seems that the latter technique would generate more waves since the grid is preferentially entraining light fluid into regions of heavier fluid as it progresses through the tank. Dickey & Mellor (1980) observed some strong oscillations in the velocity fields at large times which indicate a strong internal wavefield. The data discussed in §4.1 provided substantial evidence that SHV's data (R23) also contained a strong wavefield near the grid. Both experiments imply that, until all turbulent motions have been suppressed by buoyancy ($\overline{\rho w} \approx 0$), both longitudinal and vertical velocity fluctuations (turbulence and wave components) decay at the same (or even slower) rate than for a neutral flow. Then, both velocity components decay very slowly with large oscillations, which can be attributed to an internal wavefield. These measurements (R23) could wrongly be interpreted as a rapid collapse of the turbulence if it is assumed that no significant amount of internal waves were present throughout the evolution of the turbulence. Therefore, an operational way to separate internal waves from the turbulent velocity fluctuations is required.

5.2. *Influence of upstream fluctuations*

Stillinger (1981) determined that the velocity fluctuations upstream of his grid were significant and resulted from the incomplete suppression of the ten mixing layers at the UCSD water-channel test-section entrance. The measurements reported herein probably also contain significant upstream velocity fluctuations although extensive measurements to examine this question have not been made for the present configuration of the water channel. The sizeable upstream velocity fluctuations may inhibit direct comparisons with classical homogeneous grid measurements in wind tunnels or with towed-grid measurements. While we can expect some deviation from the classical velocity decay, the upstream *velocity*-fluctuation noise is really a true fluid-mechanical signal and as such will not cause fundamental problems in interpreting the decay of turbulence in the stratified flow downstream of the grid. The grid and the upstream fluctuations should be considered to be a combined source of turbulence. The detailed results of the downstream turbulence and buoyancy interactions (exponent in the decay laws for instance) may be somewhat different because of the combined turbulence source, but the physics of the energy decay should not be very

sensitive to the way in which the turbulence is generated except for the possible preferential formation of internal waves instead of turbulence in some cases. We attempt to deal with this particular problem, which appears only for the small grid (SHV and R52), in the following section. It would not be very useful to subtract this fluid-dynamical noise signal for the stratified turbulence decay as one might do for electronic or vibrational noise sources because of the importance of the strong nonlinear interaction between the upstream velocity fluctuations, the grid rods and the stable stratification.

5.3. *Turbulence–wave separation*

It is useful to attempt to decompose the velocity field into a mean velocity, a turbulent fluctuation and a wave fluctuation. This decomposition may also be interpreted as a lengthscale decomposition of the ranges of internal-wave lengthscales and turbulent lengthscales are distinctly separated. This separation may be more clearly approximated in high-Reynolds-number flows such as atmospheric and oceanic flows than in low-Reynolds-number laboratory flows where there is no inertial subrange. Good examples of this separation in which a clear spectral gap appears between wave and turbulent components may be found in the oceanic vertical-shear spectrum of Gargett *et al.* (1981) and in the atmospheric surface-layer-velocity measurements of Högström & Högström (1975). While there is no spectral gap in our lower-Reynolds-number flows, the correlation between differences in behaviour noted for high- and low-frequency ranges and the energy decay rates suggests that a similar wave–turbulence decomposition may be useful. It seems unlikely that waves and three-dimensional turbulence can coexist at the same scales with comparable energy levels. Therefore it is reasonable to neglect the turbulence–wave interaction and assume that the wave fluctuation and the turbulent fluctuation are statistically independent. Then the vertical r.m.s. velocity w' can be decomposed as:

$$w'^2 = w_t'^2 + w_w'^2, \tag{20}$$

where w_t' is the vertical r.m.s. turbulent velocity and w_w' the vertical r.m.s. wave velocity. It has been shown in §4.1 that for small internal-wave contribution ($w_w' \ll w_t'$), the Ozmidov scale L_O is related to the buoyancy scale L_b by a power law of the type

$$L_O = CL_b^m, \tag{21}$$

where C and m are constants depending on the grid geometry. In terms of the vertical velocity (21) becomes:

$$w_t' = N\left(\frac{L_O}{C}\right)^{1/m}. \tag{22}$$

When the three-dimensional turbulence has been suppressed by buoyancy effects or when the level of internal waves is significant, we have:

$$L_O \ll CL_b^m \quad \text{or} \quad w' \gg w_t'. \tag{23}$$

Then, the vertical wave velocity can be estimated as:

$$w_w' = N\left[L_b^2 - \left(\frac{L_O}{C}\right)^{2/m}\right]^{\frac{1}{2}}. \tag{24}$$

Figure 13 shows the evolution of the estimated vertical turbulent intensity squared $w_t'^2/\overline{U}^2$ compared with the total velocity intensity for the three stratifications of R23. It is apparent that the estimated turbulent vertical velocity w_t' of the small-M grid

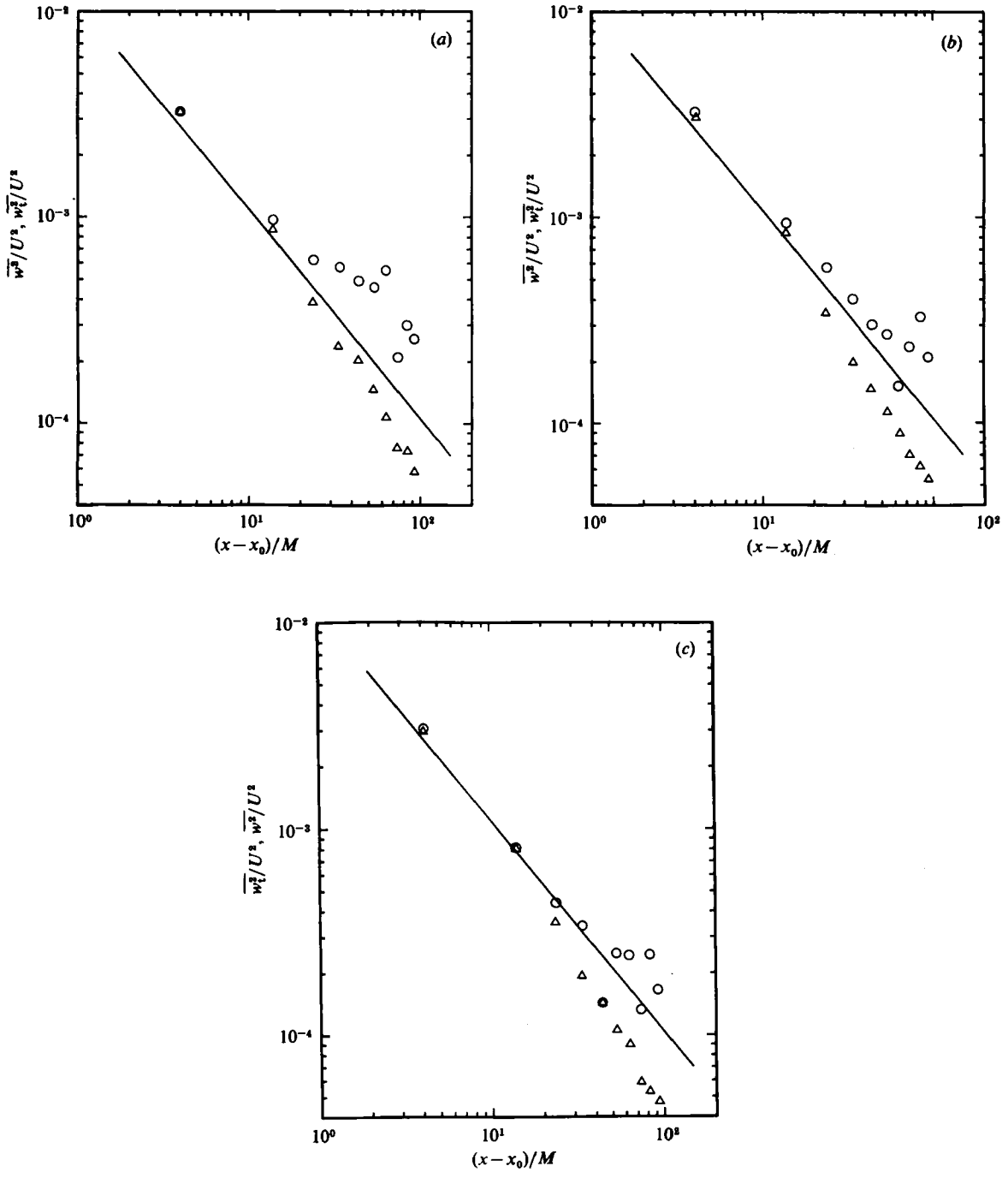

FIGURE 13. Comparison between the total vertical velocity fluctuation $\overline{w^2}/U^2$ (○) and the vertical turbulent fluctuation $\overline{w_t^2}/U^2$ (△) estimated from (24) for SHV's data (1983) *vs.* downstream distance from the grid ($x_0/M = 6$) for their three stratifications. The solid line refers to the corresponding vertical velocity decay without any stratification; (*a*) $N = 0.95$ rad/s, (*b*) 0.73, (*c*) 0.45.

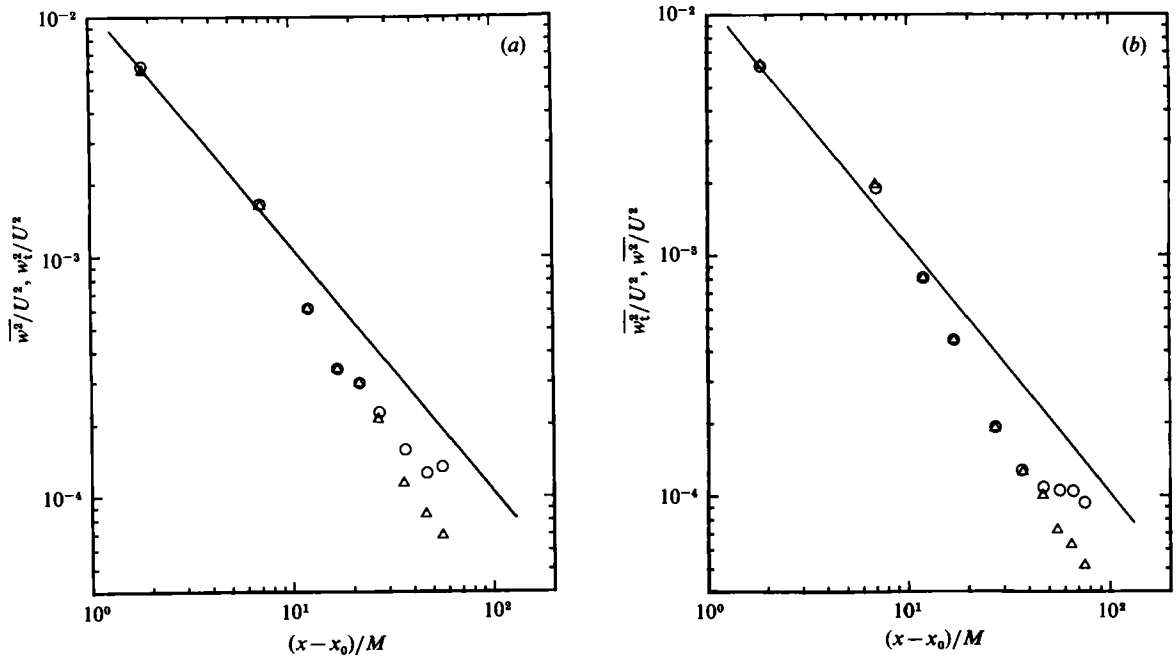

FIGURE 14. Comparison between the total vertical velocity fluctuation $\overline{w^2}/U^2$ (○) and the vertical turbulent fluctuation $\overline{w_t^2}/U^2$ (△) estimated from (24) for two stratifications of the present data (R37) *vs* downstream distance from the grid ($x_0/M = 3.2$). The solid line refers to the corresponding vertical velocity decay without any stratification; (*a*) $N = 0.98$ rad/s, (*b*) 0.44.

x/M	w' from SHV (1983) (cm/s)	w_t' from (22) (cm/s)	w_w' from (24) (cm/s)	w_t' from figure 19 (cm/s)	w_w from figure 19 (cm/s)
20	0.724	0.689	0.222	0.649	0.320
40	0.560	0.362	0.427	0.444	0.342
60	0.509	0.287	0.420	0.333	0.383
80	0.357	0.215	0.285	0.257	0.24
100	0.399	0.192	0.350	0.236	0.323

TABLE 6. Separation of the vertical velocity into internal-wave and turbulent components using the criterion of (22) and the spectral cut-off at the low wavenumbers described in figure 19; R23 (SHV, 1983), $N = 0.97$ s^{-1}

data of SHV (and R52 as well) is decaying at a faster rate under the effects of buoyancy in much the same way as the large-M data (R36 and R37) of figure 14. The determination of the decay rate of w'/U of buoyancy-dominated turbulence is very sensitive to the choice of the virtual origin x_0. In figures 13 and 14, x_0 was chosen to be the virtual origin for the neutral-case ($N = 0$) decay in order to stress the effects of stabilizing buoyancy forces. For the small-M-grid data of R23 the vertical internal-wave velocity estimated from (24) is $w_w' \approx 0.30$ cm/s for all x/M greater than 10, as illustrated in table 6, while for the large-M-grid data (R37) the estimated vertical velocity of the internal wavefield is significant only after the extinction of turbulence (complete fossilization) and has an average value of only 0.15 cm/s.

6. Dissipation rate of density fluctuations

6.1. *Estimates of χ and Cox number*

The spatial resolution of the MSCI was adequate for resolving the full range of wavenumbers contributing to the mean-square density fluctuations. However, owing to the small molecular diffusivity of salt, the resolution was not adequate to resolve the higher wavenumbers providing the major contribution to the mean-square fluctuating density gradient $(\overline{\partial\rho/\partial x_i})(\overline{\partial\rho/\partial x_i})$ and dissipation rate of density fluctuations

$$\chi = 3D\left(\overline{\frac{\partial\rho}{\partial x_i}\frac{\partial\rho}{\partial x_i}}\right),$$

where D is the molecular diffusivity of salt. However, since all the terms except χ in the budget equation of mean density fluctuations were measured, χ could be calculated from this equation as

$$\chi = -\bar{U}\frac{\partial\overline{\rho^2}}{\partial x} - 2\overline{\rho w}\frac{\partial\bar{\rho}}{\partial z}. \tag{25}$$

Some assessment of the accuracy of this method and the accuracy of the assumption of homogeneity for the present data was obtained by comparing the degree of balance of the terms in the equation for the fluctuating velocity:

$$\bar{U}\frac{\partial}{\partial x}\frac{\overline{q^2}}{2} = -\frac{g}{\bar{\rho}}\overline{\rho w} - \epsilon, \tag{26}$$

for which all the terms except $\overline{v^2}$ were directly measured. Assuming $\overline{v^2} = \overline{u^2}$ and numerically integrating to obtain $\overline{q^2}$, the balance of (26) was found to hold within 5% over the entire range of x/M when all the terms in (26) were integrated from the largest to the smallest values of x/M. This *backwards* integration was necessary to evaluate the balance because of the relatively sparse data for the smallest values of x/M where the changes in the variables occur most rapidly. An example of the data (R36, $N = 0.90$ rad/s) for the gradient term $\bar{U}(\partial\overline{\rho^2}/\partial x)$ computed by numerical differentiation of curve fits to ρ^2 *versus* x, the corresponding buoyancy-flux term (second term on the right-hand side of (25)), and the deduced values of χ obtained from (25), are shown in figure 15. χ increases for small x/M, rapidly rising to a maximum value, and then monotonically decays with x/M. The maximum in χ occurs at roughly the same x/M location as the maximum in $\overline{\rho^2}$.

The dimensionless scalar dissipation rate $\chi/(D(\partial\bar{\rho}/\partial z)^2)$ is equal to twice the *isotropic* Cox number $Co = 3\overline{(\partial\rho/\partial z)^2}/(\partial\bar{\rho}/\partial z)^2$, a parameter frequently used to characterize turbulent mixing in recent discussions of ocean-microstructure measurements. In oceanographic measurements the Cox number is defined as the ratio between the vertical eddy diffusivity and the molecular diffusivity. The higher the Cox number, the more vigorous the turbulent mixing.

The variation of the Cox number with x/M is similar to that of χ. However, as illustrated by the data for R36 and R37 given in figure 16, when plotted *versus* Nt, for values of Nt greater than unity, the Cox-number data for different values of N collapse fairly well toward a single curve. This behaviour is similar to the collapse for the mean-square density-fluctuation data normalized with the mean density gradient, as noted earlier by SHV. The Cox-number data for the different values of N for R23 ($M = 1.905$ cm) also collapse toward another single, but different, curve, which lies consistently below that for the larger-grid data by roughly a factor of 2.

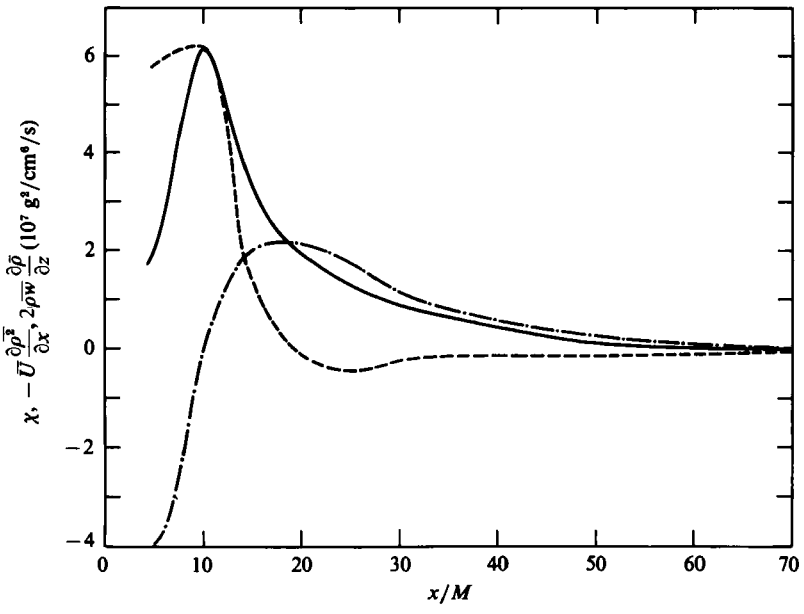

FIGURE 15. Evolution of the terms in the fluctuating potential-energy balance (25) with x/M for R36 ($N = 0.90$ rad/s): ——, χ; · · · · · ·, $(-\overline{U}\partial\overline{\rho^2}/\partial x)$; – – –, $(-2\overline{\rho w}\partial\bar{\rho}/\partial z)$.

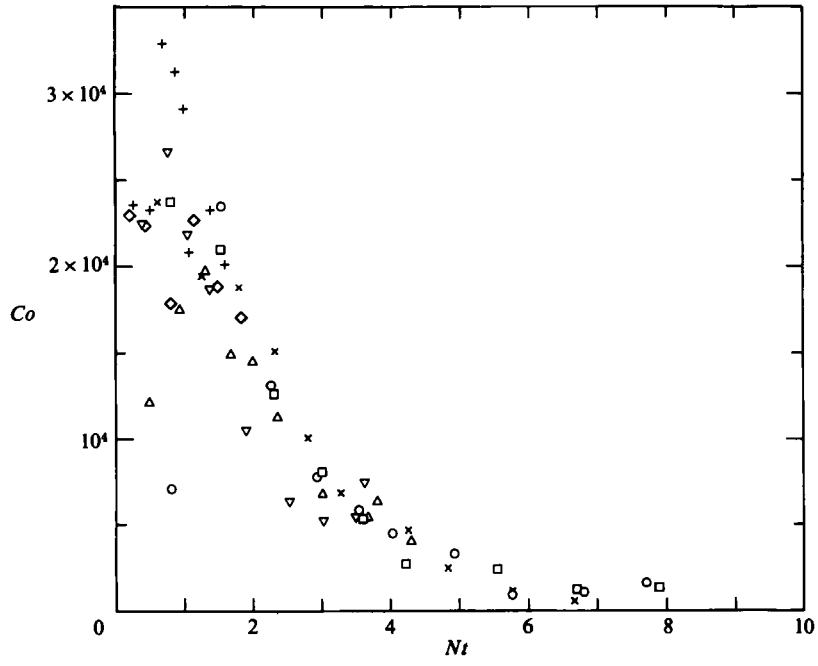

FIGURE 16. Cox number Co *vs* non-dimensional time Nt. R36: $N = 0.90$ rad/s; △, 0.56; +, 0.27. R37: □, $N = 0.98$ rad/s; ×, 0.74; ▽, 0.44; ◇, 0.24.

Thus, in both the initial build-up and buoyancy-dominated period of turbulent decay, the Cox number is found to be an increasing function of the overturning scale, and is approximately proportional to the scale of the mixing process.

The very large values of the Cox number associated with large vertical overturns observed in the oceanic temperature-microstructure measurements are consistent with this result. For example, the largest value of $Co = 280000$ found by Dillon (1982) had an overturning (Thorpe) scale $L_T = 480$ cm. These values are greater than our maximum Cox number and L_T for the large-grid data by factor of 10 and 100 respectively. For Dillon's next largest value of $Co = 170000$ and $L_T = 200$ cm, the relative ratios are about the same. The considerable difference in the inferred proportionality constant relating Co and L_T between the laboratory and the field data could be related to the difference in Schmidt number for salt and Prandtl number for temperature, but definite statements about the possible effects of Prandtl and Schmidt number may require similar laboratory measurements using heat instead of salt as the density-stratifying agent. A Cox number *versus* Nt plot like figure 16 cannot be constructed for Dillon's (1982) data, because the elapsed times since the initial stirring event are not known.

The lowest values of Co for the present data, which occur for the largest values of N and x/M, are approximately 300, a factor of about 10 larger than the smallest values (20) found in the vertical-temperature-microstructure measurement of Dillon (1982). This would imply correspondingly larger values of Nt for the microstructure data than were obtained in the present experiments if the ocean turbulence were decaying. The values of the Cox number when $\overline{\rho w} \approx 0$ range from 4500 to 9000. In the direct numerical simulations of decaying density (salt)-stratified homogeneous turbulence of Riley, Metcalf & Weissman (1981), when $\overline{\rho w} \approx 0$, Co is equal to 7500 and 3000 for $N = 1.57$ and 3.14 rad/sec respectively, in reasonable order-of-magnitude agreement with the present experiments.

6.2. *Dissipation rate at the onset of buoyancy effects*

The present indirect estimates of χ show that for homogeneous turbulence at the beginning of fossilization (see table 4) the dissipation rate $\epsilon_0 = (5.5 \pm 2) DC_0 N^2$. Direct measurements of χ would allow a better estimate of this ratio. It should be noted that in our laboratory experiments the turbulence is not in a steady state as is often assumed for the ocean.

As shown in figure 17, the laboratory data (R26 and R37) after complete fossilization ($\overline{\rho w} \approx 0$) fall below the line defined by $\epsilon_{tr} = 4D\,Co_{tr}\,N^2$. The average ratio $\epsilon_{tr}/D\,Co_{tr}\,N^2$ obtained from table 5 is 2.8 ± 1. No dependence on grid Reynolds number is apparent from the data.

Gibson (1980, 1982*b*) proposed a heuristic model for a single patch of entraining turbulence at the beginning of fossilization (onset of buoyancy effects) in a thermally stratified fluid. His first arguments assume an analogy with the case of a stably stratified laminar shear flow becoming unstable with a local Richardson number $Ri = N^2/\overline{(\partial u/\partial z)^2} = \frac{1}{4}$. Gibson deduces that the dissipation rate ϵ_0 would be in the range $(2-\frac{15}{2})\,\nu\overline{(\partial u/\partial z)^2}$ for a plane shear flow or isotropic turbulence respectively and the corresponding Cox number would be $Co_0 = 2\nu/D$. Combining these expressions leads to

$$\epsilon_0 = (4-15)\,D\,Co_0\,N^2. \tag{27}$$

Gibson (1982*b*) proposed another method to derive (27). The method consists in connecting a *fine-structure* temperature-gradient spectrum with the universal

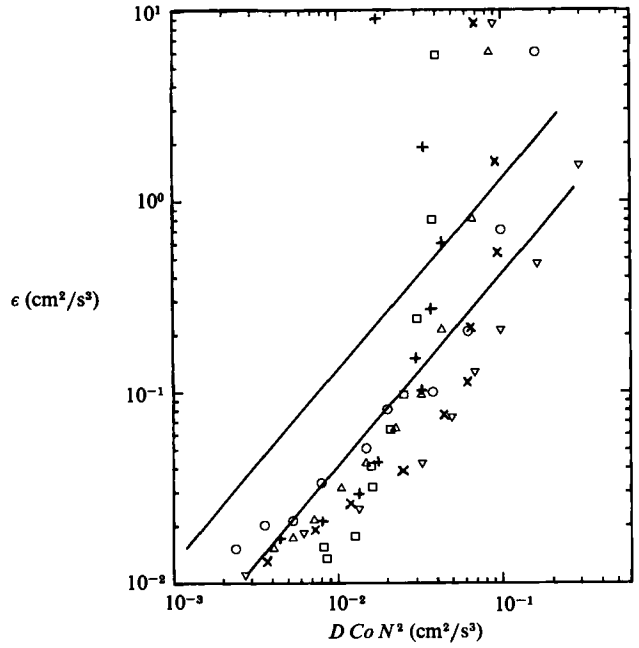

FIGURE 17. Dissipation rate ϵ *vs.* $D\,Co\,N^2$. The upper line represents Gibson's (1982*b*) estimate of the dissipation rate at the onset of buoyancy effects (beginning of fossilization): $\epsilon_0 = 13 D\,Co_0\,N^2$. The lower line $\epsilon_{tr} = 4 D\,Co\,N^2$ represents the corresponding dissipation-rate threshold from oceanic-microstructure measurements (Dillon 1984; Gregg 1984).

turbulent-scalar-gradient spectrum at the transition wavenumber $2\pi/L_O$. The resulting expression for ϵ_0 is

$$\epsilon_0 = 13 D\,Co_0\,N^2. \tag{28}$$

Dillon (1984) compared this last criterion for the existence of turbulence with the lengthscale criterion of SHV, i.e. $L_t = 0.7 L_O$, using earlier data (Dillon 1982). Dillon concluded there was some inconsistency in the definition of Gibson's activity parameter $A_T = [\epsilon/(13 D\,Co\,N^2)]^{\frac{1}{2}} = 1$ at the beginning of fossilization (onset of buoyancy effects). Agreement between these two criteria would be reached if $A_T \approx 0.5$ or equivalently if $\epsilon_0 \approx 3.25 D\,Co_0\,N^2$. A crucial assumption Dillon (1984) had to make in his derivation was to equate the available potential energy in the fluctuations (APEF, defined as the potential-energy difference between the instantaneous density profiles and the corresponding rearranged stable profiles) with the potential energy measured at a single point in time (SHV). The APEF is an upper bound for the actual available potential energy at the time of the measurements and therefore his value of the dissipation rate at the beginning of fossilization could be an underestimate. Direct comparison between the two potential energies should be made in the laboratory to answer this question.

Independently, Oakey (1982) parameterized the observed correlation between ϵ and χ in terms of a mixing efficiency η:

$$\eta = \tfrac{1}{2} g\alpha \frac{\chi}{\epsilon(\partial\bar{T}/\partial z)}, \tag{29}$$

where α is the thermal expansion coefficient of water. Equation (29) can be rewritten in terms of the Cox number Co and the Brunt–Väisälä frequency N by assuming no salinity dependence of the density profile, as

$$\eta = \frac{D\,Co\,N^2}{\epsilon}. \tag{30}$$

Oakey (1982) obtained a mixing efficiency $\eta = 0.235 \pm 0.14$. Other estimates by diverse methods yield values of 0.30 (Lilly, Waco & Adelfang 1974), 0.20 (Osborn 1980) and 0.21–0.22 (Gregg 1984). If one assumes a mixing efficiency of $\frac{1}{4}$ (McEwan 1983) when buoyancy effects start to become important, (30) yields

$$\epsilon_0 = 4D\,Co_0\,N^2. \tag{31}$$

Equation (29) provides an upper bound for the mixing efficiency since it assumes a steady state, i.e. that buoyancy flux is equal to dissipation. Direct measurements of the mixing efficiency in a decaying grid-generated turbulence by Rohr *et al.* (1984) show that the average mixing efficiency at the beginning of fossilization (onset of buoyancy effects) is 0.14.

For the direct Navier–Stokes simulations of Riley *et al.* (1981), the ratio $\epsilon/D\,Co\,N^2$, when $\overline{\rho w} \approx 0$, is 1.1 to 1.2, somewhat smaller than the range of experimental values. This difference is probably not significant, as this value is probably highly dependent on the initial conditions as discussed earlier in connection with the velocity measurements.

7. Spectral evolution of kinetic and potential energies

SHV discussed some of the spectral properties of vertical velocity fluctuations in their decaying stratified turbulent flow. They pointed out that the velocity spectra deviated from the spectral form of an unstratified turbulent flow over a range of wavenumbers whose upper limit ($k_0 = 1/1.4L_0$) increased with increasing distance from the grid. The largest scales of the turbulence are the first to be suppressed by the action of buoyancy forces and, as the spectra evolve, most of the smaller scales also become progressively dominated by buoyancy. We have further examined the velocity spectra of R23 (SHV) as well as the new data of R36, R37 and R52. The unscaled velocity spectra of both longitudinal and vertical components are compared in figure 18 at various downstream distances from the grid for the small (R52) and large (R36) mesh grids. The strongest stratification for each experiment was selected in figure 18 to emphasize the effect of stabilizing buoyancy forces on the shape of the spectra. The same conclusions are reached when the data of R23 and R37 are used. The small-mesh-grid ($M = 1.905$ cm) spectra (figures 18*a*, *b*) exhibit a very distinct steep slope varying as k^{-2} at the low-wavenumber end of the spectra. This region does not decay as one goes further away from the grid as does the high-wavenumber end of the spectra. The SHV velocity spectra for R23 contained an identical change in slope at small wavenumbers to that observed for the other small-M-grid data of R52. In contrast, the large-M-grid velocity spectra of R36 (as well as R37 not shown for briefness) exhibit a flat low end which is typically found in most unstratified spectral measurements. The calculations of §5.3 suggest, as does the steep slope of the small-M-grid spectra at small wavenumbers, that this region may be dominated by internal-wave motions (a k^{-2} slope in the spectra corresponds to a saturated two-dimensional internal wavefield), while the large-M-grid spectra

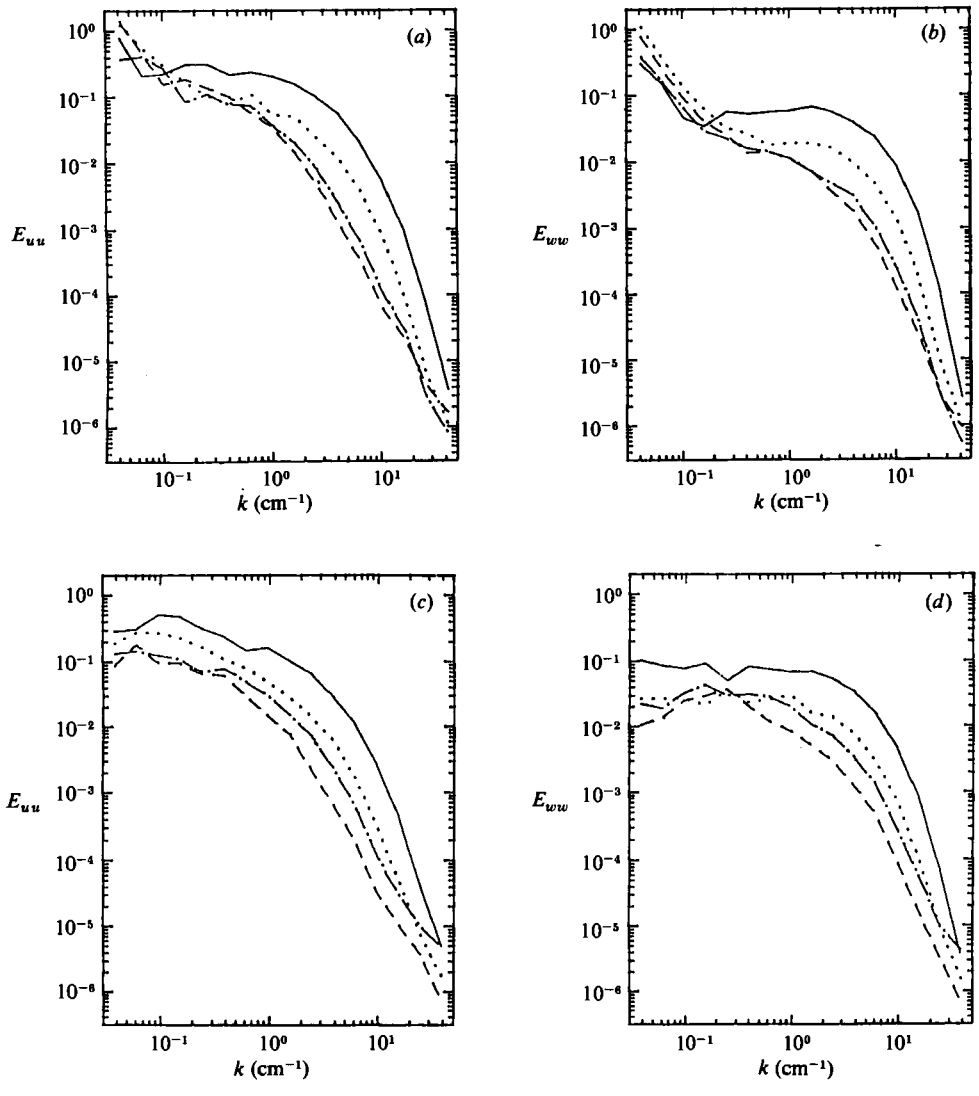

FIGURE 18. Horizontal and vertical velocity spectra for the small-M grid (R52) and the large-M grid (R36) at various x/M. (*a*) u, (*b*) w; R52, $M = 1.905$ cm, $N = 0.93$ rad/s. (*c*) u, (*d*) w; R36, $M = 3.81$ cm, $N = 0.90$ rad/s. ——, $x/M = 20$; . . ., 40; · · · · · ·, 60; - - -, 80.

do not show internal-wave behaviour, at least over the bandwidth of the present measurements.

Figure 19 shows the results of scaling the vertical velocity spectra of R36 and R52 with the Kolmogorov scales L_{K} and $v_{\mathrm{K}} = (\epsilon\nu)^{\frac{1}{4}}$. The curves in figure 19 are a subset of the entire range of x/M and the density gradients. Many of the available spectra at small x/M where buoyancy effects are negligible are not included in order to illustrate the trends more clearly. The collapse of the scaled spectra is surprisingly good over most of the wavenumbers. This is true even for the low-wavenumber region of R52, which is probably dominated by internal waves, and the deviations at the largest wavenumbers are partly due to noise contamination from the analog tape recorder.

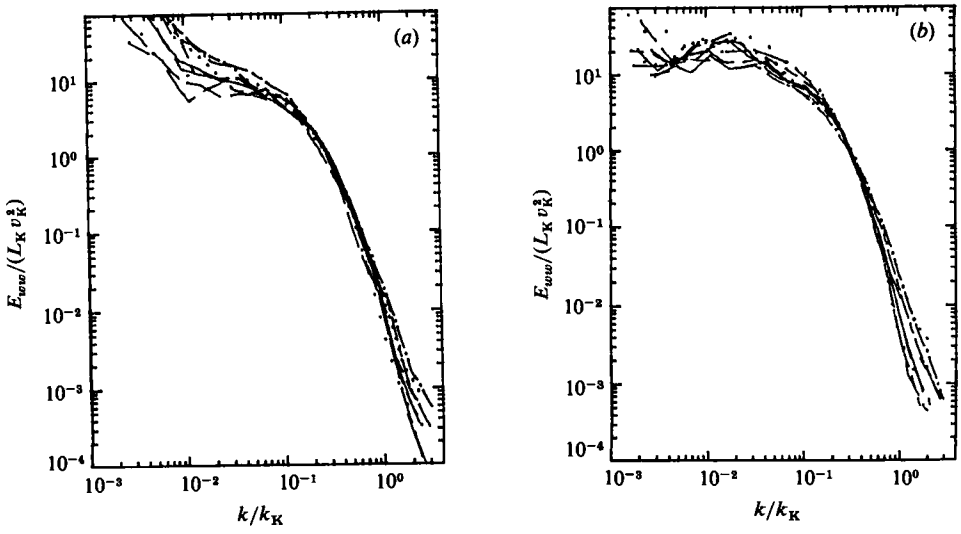

FIGURE 19. Vertical velocity spectra non-dimensionalized by Kolmogorov scales for all N at $x/M = 40$, 60, 80. (*a*) small-M grid (R52). (*b*) large-M grid (R36).

The results for R23 analysed in this manner are identical to the result for R52. It should be pointed out that none of the spectra (for which the turbulent part is buoyancy dominated) presented in figure 19 have the classical shape of nearly isotropic unstratified grid-turbulence spectra. This observed different spectral shape might be a result of a modified energy cascade to smaller scales as the energy-supplying eddies are being affected by buoyancy forces. Similar trends are also seen in the Kolmogorov-scaled horizontal velocity spectra for all the experiments, and, for the sake of briefness, are not shown here. The success of the Kolmogorov scaling over the wide range of density gradients is probably due to the range of wavenumbers used in the data analysis. The very small wavenumbers, say with $k < N/U$, would probably not show this degree of collapse. We have not yet been able to obtain measurements at very small wavenumbers because of the limitations of the hot-film instrumentation in the presence of air bubbles. There is hope that we will be able to extend our bandwidth to at least a decade lower in wavenumber in future measurements by eliminating sources of entrained air in the flow which later accumulates on the film sensors and causes a slow drift. Apparently the Kolmogorov-scaled spectra at large wavenumbers are not sensitive indicators of active scalar buoyancy forces, even when the criterion for overturning turbulence indicates that no classical Kolmogorovian turbulence remains, e.g. when $x/M > 50$ for R52.

An attempt to spectrally separate wave fluctuations and turbulent fluctuations in the vertical velocity component for SHV's data (R23) was made by decomposing the spectra into two regions as shown in figure 20. We define the *wave* contribution to the variance as that part of the spectra to the left of the flat region (dotted line) and the *turbulence* contribution as everything to the right of the low-wavenumber rise of the spectra. A more refined separation might be to use the internal-wave shape proposed by Gibson (1980), which is shown in figure 20 by a dot–dash line. Gibson (1980) proposed that the small-scale internal-wave spectrum goes as $\Phi(k) \approx \nu^{\frac{1}{2}} N^{\frac{3}{2}} k^{-2}$ with a viscous cutoff at the buoyancy analogue of the Kolmogorov scale, $L_{KF} = (\nu/N)^{\frac{1}{2}}$. Gibson's (1980) internal-wave spectral shape gives a wave-velocity variance which is about 10 % higher than the variance obtained with the sharp cut-

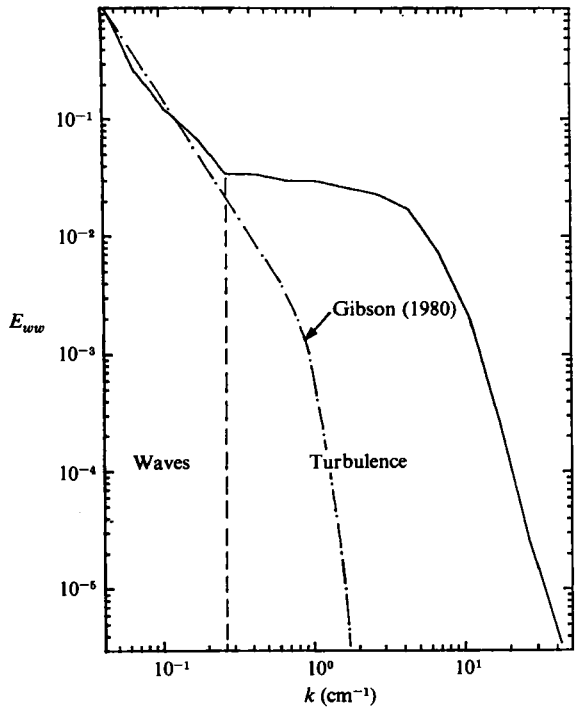

FIGURE 20. Spectral separation of internal waves and turbulence (R23, $x/M = 20$, $N = 0.97$ rad/s: $\cdots$, small-scale internal-wave spectrum proposed by Gibson (1980).

off as shown in figure 20. The spectral estimates of wave and turbulent vertical velocities for the first decay ($N = 0.97$ s^{-1}) of R23 shown in table 6 are in good agreement with the estimates obtained from the variance calculations of §5.3 ((22) and (24)) using a different method.

Figure 21 shows the results of scaling the density spectra of R23 and R36 with the Batchelor scales for various x/M and N. We used R23 instead of R52 for this comparison because the scaling depends strongly (first power) on the estimate of the scalar dissipation rate χ and the χ estimates by the indirect technique described in §6.1 appear to be quite good for R23 and R36. The collapse of the density spectra does not appear to be as good as observed for the Kolmogorov-scaled velocity spectra. This result is probably not too surprising given that the Batchelor scaling is expected to work only for a passive scalar, and not for the buoyancy-dominated flows discussed here. It is apparent that even near the grid, where buoyancy forces are dominated by inertial forces, the collapse of the density spectra with the Batchelor scales is not very good. One might have expected buoyancy effects to be negligible for the small-x/M data and that density, even for the large values of N in these measurements, would behave as a passive scalar. This conclusion must also be regarded as somewhat tentative because of the uncertainty in the χ-measurements.

Both velocity and density spectra are in excellent agreement when the Kolmogorov and Batchelor scalings are applied across the range of N, but limited to the same x/M. The scaled density spectra do exhibit a wider scatter even under these conditions at large x/M, but the uncertainty in χ at this point is at its greatest. The direct estimates of ϵ are more reliable and this may explain the better collapse of the velocity as compared to the density spectra. Improved density scaling may require direct

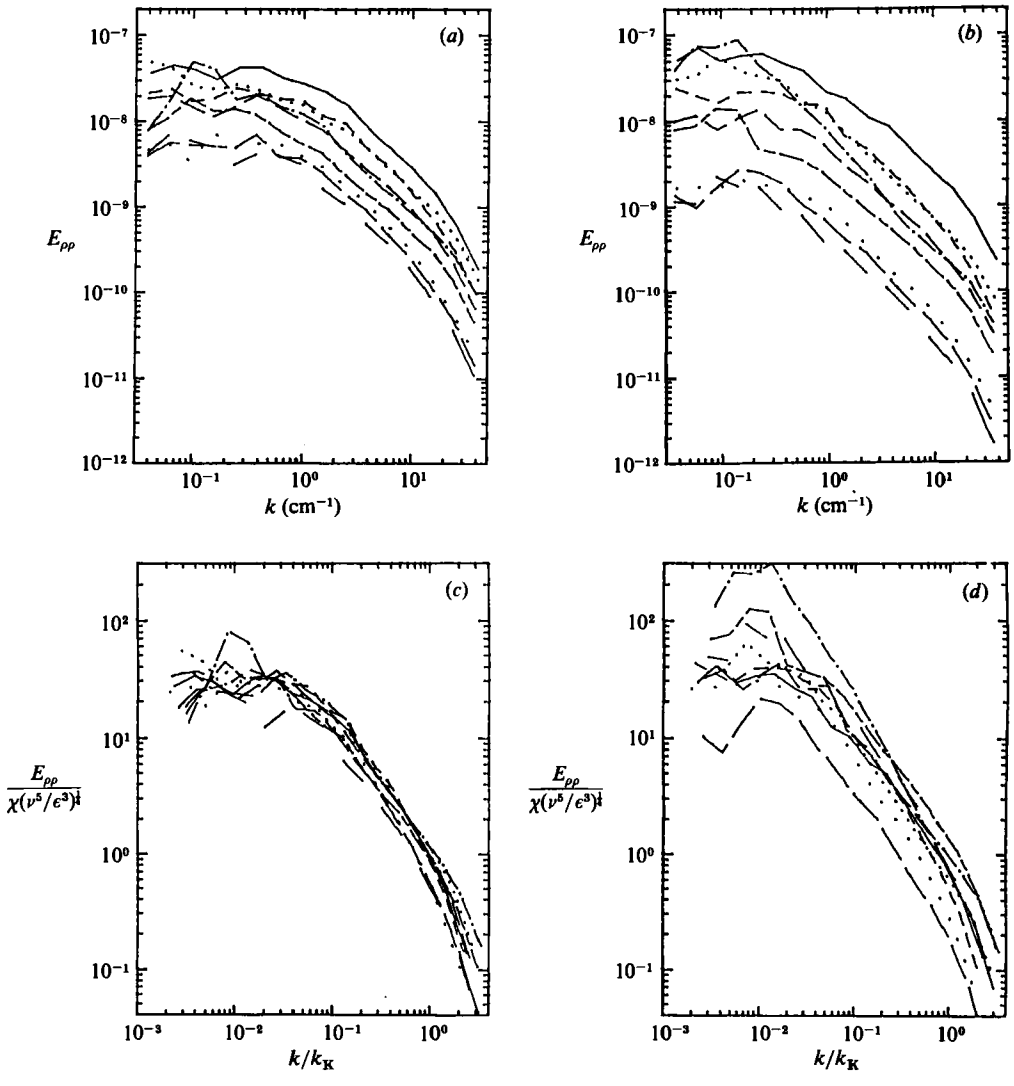

FIGURE 21. Density spectra in dimensional form and non-dimensionalized by the Batchelor scales for both grids at $x/M = 40, 60, 80$. (*a*) small-M grid (R23). (*b*) large-M grid (R36). (*c*) small-M grid (R23) in Batchelor coordinates. (*d*) large-M grid (R36) in Batchelor coordinates.

χ-measurements, a very difficult problem for salt-stratified solutions because of the small probe spatial resolution required.

Another non-dimensional scaling (to collapse the low-wavenumber region of buoyancy-influenced velocity spectra) was proposed by Gargett *et al.* (1984, hereinafter referred to as GON). They assumed that the only two relevant parameters for the scaling of energy-containing (large-scale) eddies of buoyancy-dominated turbulent flow were the ambient stratification N and the dissipation rate ϵ representing the energy cascade from these large-scale eddies to the small viscous scales. A dimensional analysis similar to the Kolmogorov scaling yields a buoyancy wavenumber $k_b = 1/L_O = (N^3/\epsilon)^{\frac{1}{2}}$ and velocity scale $u_b = (\epsilon/N)^{\frac{1}{2}}$. Replacing ν in the Kolmogorov scaling by N is equivalent to considering the buoyancy timescale $1/N$ instead of the

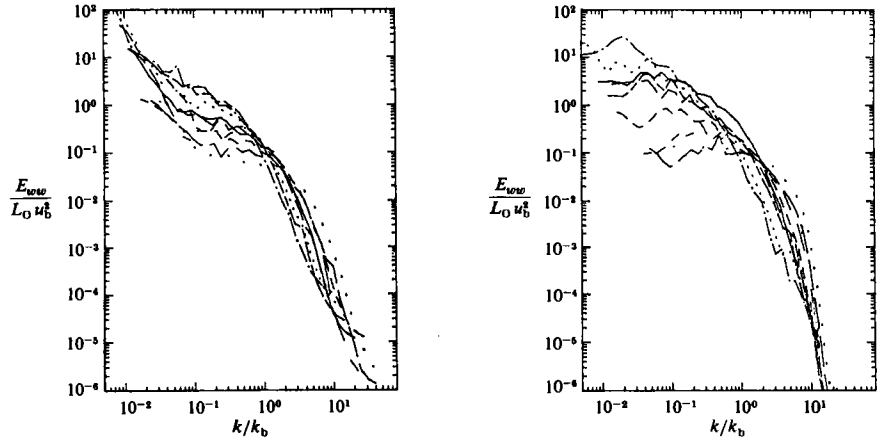

FIGURE 22. Vertical velocity spectra in the buoyancy coordinates proposed by Gargett, Osborn & Nasmyth (1984) for all N at $x/M = 40$, 60, 80. (*a*) small-M grid (R52). (*b*) large-M grid (R36).

usual turbulent timescale $(\nu/\epsilon)^{\frac{1}{2}}$. Figure 22 shows the results of applying the buoyancy length and velocity scales proposed by GON. The results in figure 22 suggest that, at least over the range of wavenumbers investigated in the laboratory flow, the GON buoyancy scaling does not collapse the spectra but rather it tends to separate them. The ordinary Kolmogorov scaling seems to do a better job of collapsing the velocity spectra. Similar results were found for the other experiments (R37 and R52). It would of course be interesting to try this approach for wavenumbers less than N/U, wavenumbers which are not obtained in the existing data sets.

8. Conclusions

The present experiments on the decay of homogeneous turbulence in a stably stratified fluid confirm the overall results of SHV with some important differences, which can be related to different initial conditions. The lengthscale model proposed by Gibson (1980) and SHV is shown to describe adequately the state of fluid motion throughout its evolution from a Kolmogorovian turbulence to a composite of internal waves and fossil turbulence (or quasi-two-dimensional turbulence). SHV's data have been re-examined and some adjustment of the proportionality constants between the various relevant scales made. It is shown that the largest turbulent scale L_t allowed by buoyancy is $L_t = 0.85L_O$ for both grid mesh sizes. On the other hand the ratio between the Ozmidov scale L_O and the Kolmogorov scale L_K, which determines the smallest turbulent scale of the flow, appears to depend on the Reynolds number. In other words, the transition dissipation rate ϵ_{tr} below which no overturning turbulence can exist varies from $15\nu N^2$ for the small-M grid to $21\nu N^2$ for the large-M grid. A small increase in ϵ_{tr} with grid Reynolds number is observed. More experiments at different Reynolds numbers need to be performed in order to be more conclusive. A word of caution has to be exercised when comparing decaying grid turbulence with oceanic turbulence because the generating mechanisms could be very different. For example, Thorpe (1984) has recently suggested that, in the ocean, turbulence due to Kelvin–Helmholtz instability may be produced by secondary instabilities and not a collapse of the primary Kelvin–Helmholtz billows. While Kelvin–Helmholtz billows have been observed in the ocean (Woods 1968) it is not known whether they are a

dominant mechanism for generating ocean turbulence through either primary or secondary instabilities, or whether the resulting turbulence differs significantly from decaying laboratory grid turbulence. While the details of a truly three-dimensional turbulence might not be dependant on its origins, the very weak source of turbulence caused primarily by secondary instabilities might have some different quantitative properties compared with stronger sources of turbulence such as the collapse of the primary Kelvin–Helmholtz billow itself.

Estimates of the scalar dissipation rate χ show that the Cox number is an increasing function of the overturning scale L_t. Large values of Cox number correspond to large overturning scales, in agreement with oceanic microstructure measurements (Dillon 1982). From the Cox-number estimates the criterion for the onset of buoyancy effects (begining of fossilization) can be written in terms of a minimum dissipation rate ϵ_0. Turbulence is first affected by buoyancy forces when $\epsilon < \epsilon_0 \equiv (5.5 \pm 2)\, D\, Co\, N^2$. The dissipation rate $\epsilon_0 = 13 DCN^2$ proposed by Gibson (1982*b*) for a single turbulent patch is a factor of 2.4 larger while the estimate $\epsilon_0 \approx 4 D\, Co\, N^2$ from Oakey (1982), Dillon (1984) and Gregg (1984) is 25% smaller. In the present laboratory experiments it appears that all turbulence has been suppressed ($\overline{\rho w} = 0$) when $\epsilon < 2.8 D\, Co\, N^2$, independent of the grid mesh size.

The major difference between the present experiments, and those of SHV and the towed-grid experiments (Lin & Veenhuizen 1975; Dickey & Mellor 1980; Britter *et al.* 1983) is in the evolution of the velocity fluctuations. It appears that the decay rate of the horizontal kinetic energy ($\overline{u^2} \approx x^{-1}$) is basically unaffected by buoyancy effects, while the rate of decay of the vertical kinetic energy is faster ($\overline{w^2} \approx x^{-1.4}$) when buoyancy forces suppress the largest scales. This increased decay rate does not seem to depend on the stratification as long as the turbulence is buoyancy dominated. These results are in good agreement with Lin & Veenhuizen (1975). Some caution has to be used when comparing the towed- and untowed-grid measurements because of the larger upstream fluctuation levels in the latter case. The effect of the large upstream velocity fluctuations probably leads to somewhat different decay parameters, but the transitional properties of the flow due to buoyancy forces should not be affected. Britter *et al.* (1983) observed a reduction in the vertical velocity only but no increase in its decay rate. It should be pointed out that, by the criteria of Gibson (1980) and the SHV lengthscale model, the Britter *et al.* (1983) flow was dominated by buoyancy forces upstream of their first measuring station, which appears to explain why they always observed $\overline{w^2}$ values smaller than for the unstratified case. We have found no satisfactory explanation for why they did not observe a faster decay rate for $\overline{w^2}$, but we noted that inhomogeneities in the flow could make measurements of small vertical velocities with a *Taylor diffusion* probe very uncertain. A direct comparison of all the experiments performed in the UCSD water channel showed that, for the small-M-grid case (SHV and R52), the flow contains a significant internal wavefield which dominates the behaviour of the velocity fluctuations as the turbulent components are suppressed by buoyancy. Two techniques were used to decompose the total vertical velocity into wave and turbulent components. As a result the *true* turbulent component appears to decay at a faster rate than for the unstratified case, in agreement with all the large-M-grid data and Lin & Veenhuizen (1975). The small-scale internal-wave component can be associated with a rise ($\propto k^{-2}$) in the low-wavenumber end of the velocity spectra. This interpretation also suggests that the grid Dickey & Mellor (1980) dropped in their tank generated a strong internal wavefield that dominated the evolution of the total velocity fluctuations. However, as pointed out by a referee, quantitative interpretation of the Dickey & Mellor (1980)

data in this respect is impeded by the fact that their optical technique has a poor signal-to-noise ratio when the velocity fluctuations are small. The fluctuating index of refraction of the salt solution produces an error in the measured velocity whose estimation requires a number of assumptions and knowledge of the density fluctuations, which were not measured.

Comparisons of velocity and density spectra for different stratifications and downstream distance from the grid show that Kolmogorov and Batchelor scalings collapse the spectra better than a buoyancy scaling (GON). It should be pointed out that when buoyancy forces dominate inertial forces the spectral shape of the velocity components is different from the shape of isotropic velocity spectra. These conclusions should be taken with caution given that the range of wavenumbers obtained in the present experiments did not include either low-frequency internal waves on scales greater than U/N or small density scales of the order of the Batchelor scale for direct estimates of the scalar dissipation rate.

The authors wish to thank C. H. Gibson, J. J. Rohr and D. C. Stillinger for many fruitful discussions. Funding for this work was provided by the National Science Foundation under Grants OCE82-05946 and MEA81-00431.

REFERENCES

BATCHELOR, G. K. & TOWNSEND, A. A. 1948 Decay of isotropic turbulence in the initial period. *Proc. R. Soc. Lond.* A **193**, 539.

BRITTER, R. E., HUNT, J. C. R., MARSH, G. L. & SNYDER, W. H. 1983 The effect of stable stratification on turbulent diffusion and the decay of grid turbulence. *J. Fluid Mech.* **127**, 27.

CALDWELL, D. R. 1983 Oceanic turbulence: big bangs or continuous creation? *J. Geophys. Res.* **88**, 7543.

CASTALDINI, M., HELLAND, K. N. & MALVESTUTO, V. 1980 Hot-film anemometry in aqueous NaCl solutions. *Intl J. Heat Mass Transfer* **24**, 133.

DICKEY, T. D. & MELLOR, G. L. 1980 Decaying turbulence in neutral and stratified fluids. *J. Fluid Mech.* **99**, 13.

DILLON, T. M. 1982 Vertical overturns: a comparison of the Thorpe and Ozmidov scales. *J. Geophys. Res.* **87**, 9601.

DILLON, T. M. 1984 The energetics of overturning structures: implications for the theory of fossil turbulence. *J. Phys. Oceanogr.* **14**, 541.

DILLON, T. M. & CALDWELL, D. R. 1980 The Batchelor spectrum and dissipation in the upper ocean. *J. Geophys. Res.* **85**, 1910.

ELLISON, T. H. 1957 Turbulent transport of heat and momentum from an infinite rough plane. *J. Fluid Mech.* **2**, 456.

GARGETT, A. E., HENDRICKS, P. J., SANFORD, T. B., OSBORN, T. R. & WILLIAMS, A. J. 1981 A composite spectrum of vertical shear in the upper ocean. *J. Phys. Oceanogr.* **11**, 1258.

GARGETT, A. E., OSBORN, T. R. & NASMYTH, P. W. 1984 Local isotropy and the decay of turbulence. *J. Fluid Mech.* **144**, 231.

GIBSON, C. H. 1980 Fossil temperature, salinity and vorticity in the ocean. In *Marine Turbulence* (ed. J. C. T. Nihoul), p. 221. Elsevier.

GIBSON, C. H. 1982*a* Alternative interpretations for microstructure patches in the thermocline. *J. Phys. Oceanogr.* **12**, 374.

GIBSON, C. H. 1982*b* On the scaling of vertical temperature spectra. *J. Geophys. Res.* **87**, 8031.

GREGG, M. C. 1980 Microstructure patches in the thermocline. *J. Phys. Oceanogr.* **10**, 915.

GREGG, M. C. 1984 Persistent turbulent mixing and near-inertial internal waves. In *Proc. 2nd 'Aha Huliko'a Hawaiian Winter Workshop.*

HEAD, M. J. 1983 The use of miniature four-electrode conductivity probes for high resolution measurement of turbulent density or temperature variations in salt-stratified water flows. Ph.D. thesis, University of California, San Diego.

HÖGSTRÖM, A. S. & HÖGSTRÖM, U. 1975 Spectral gap in surface layer measurements. *J. Atmos. Sci.* **32**, 340.

ITSWEIRE, E. C. 1984 Measurements of vertical overturns in a stably stratified turbulent flow. *Phys. Fluids* **27**, 764.

LANGE, R. E. 1982 An experimental study of turbulence behind towed biplanar grids in a salt-stratified fluid. *J. Phys. Oceanog.* **12**, 1506.

LESIEUR, M. & HERRING, J. R. 1985 Diffusion of a passive scalar in two-dimensional turbulence. *J. Fluid Mech.* **161**, 79.

LILLY, D. K., WACO, D. W. & ADELFANG, S. I. 1974 Stratospheric mixing estimated from high-altitude turbulence measurements. *J. Appl. Met.* **13**, 488.

LIN, J. T. & PAO, Y. H. 1979 Wakes in stratified fluids. *Ann. Rev. Fluid Mech.* **11**, 317.

LIN, J. T. & VEENHUIZEN, S. D. 1975 Measurements of the decay of grid-generated turbulence in a stratified fluid. *Flow Research Note no.* 85.

MCEWAN, A. D. 1983 The kinematics of stratified mixing through internal wavebreaking *J. Fluid Mech.* **128**, 47.

MONTGOMERY, R. D. 1974 An experimental study of grid turbulence in a thermally stratified flow. Ph.D. thesis, University of Michigan.

OAKEY, N. S. 1982 Determination of the rate of dissipation of turbulent energy from simultaneous temperature and velocity shear microstructure measurements. *J. Phys. Oceanogr.* **12**, 256.

OSBORN, T. R. 1980 Estimates of the local rate of vertical diffusion from dissipation measurements. *J. Phys. Oceanogr.* **10**, 83.

OZMIDOV, R. V. 1965 On the turbulent exchange in a stably stratified ocean. *Atmos. Ocean. Phys.* **8**, 853.

RILEY, J. J., METCALF, R. W. & WEISSMAN, M. A. 1981 Direct numerical simulations of homogeneous turbulence in density-stratified fluids. In *Non-linear Properties of Internal Waves* (ed. B. West). *AIP Conf. Proc.* no. 76.

ROHR, J. J., ITSWEIRE, E. C. & VAN ATTA, C. W. 1984 Mixing efficiency in stably-stratified decaying turbulence. *J. Geophys. Astrophys. Fluid Dyn.* **29**, 221.

SIRIVAT, A. & WARHAFT, Z. 1983 The effect of a passive cross-stream temperature gradient on the evolution of temperature variance and the heat flux in grid turbulence. *J. Fluid Mech.* **128**, 323.

STEWART, R. W. 1969 Turbulence and waves in a stratified atmosphere. *Radio Sci.* **4**, 1289.

STILLINGER, D. C. 1981 An experimental study of the transition of grid turbulence to internal waves in a salt-stratified water channel. Ph.D. thesis, University of California, San Diego.

STILLINGER, D. C. 1983 The interpretation of statistics from hot-film anemometers used in salt water flows of variable temperature and density. *J. Phys.* E: *Sci. Instrum.* **15**, 1322.

STILLINGER, D. C., HEAD, M. J., HELLAND, K. N. & VAN ATTA, C. W. 1983*a* A closed-loop gravity-driven water channel for density-stratified shear flows. *J. Fluid Mech.* **131**, 73.

STILLINGER, D. C., HELLAND, K. N. & VAN ATTA, C. W. 1983*b* Experiments on the transition of homogeneous turbulence to internal waves in a stratified fluid. *J. Fluid Mech.* **131**, 91.

TAVOULARIS, S. & CORRSIN, S. 1981 Experiments in nearly homogeneous turbulent shear flow with a uniform mean temperature gradient. *J. Fluid Mech.* **104**, 311.

THORPE, S. A. 1977 Turbulence and mixing in a Scottish loch. *Phil. Trans. R. Soc. Lond.* A **286**, 125.

VAN ATTA, C. W., HELLAND, K. N. & ITSWEIRE, E. C. 1984 The influence of stable stratification on spatially decaying vertically homogeneous turbulence. In *Proc. IUTAM Symposium on Turbulence and Chaotic Phenomena in Fluids, Sept. 1983, Kyoto, Japan* (ed. T. Tatsumi), p. 519. North Holland.

WOODS, J. D. 1968 Wave induced shear instability in the summer thermocline. *J. Fluid Mech.* **32**, 791.